Chemical Geology 710 (2026) 123383

Contents lists available at ScienceDirect

Chemical Geology

journal homepage: www.elsevier.com/locate/chemgeo

Research Paper

Near-concordant zircon Pb-loss array caused by melt-mediated coupled dissolution-precipitation replacement reactions: Signatures and geological significance

Jean-Antoine Gazi [a,*], Nathan R. Daczko [a], Elena Belousova [b], Jacqueline A. Halpin [c,d], Sandra Piazolo [e]

[a] School of Natural Sciences, Macquarie University, Sydney, NSW, Australia
[b] Geological Survey of Queensland, Brisbane, QLD, Australia
[c] Institute for Marine and Antarctic Studies, University of Tasmania, Hobart, TAS, Australia
[d] The Australian Centre for Excellence in Antarctic Science, University of Tasmania, Hobart, TAS, Australia
[e] School of Earth and Environment, University of Leeds, Leeds, United Kingdom

ARTICLE INFO

Editor: Claudia Romano

Keywords:
Coupled dissolution-precipitation replacement reaction
Zircon geochronology
Pb-loss
Mawson charnockite
Metamictisation

ABSTRACT

Arrays of near-concordant U—Pb zircon ages are interpreted to develop during (i) long-lived geological events involving protracted periods of zircon growth or (ii) mobilization and escape of radiogenic Pb during a secondary event. However, distinguishing between either interpretation remains challenging. In this contribution we investigate the complex geochronology of a meta-gabbro from the Mawson Charnockite plutonic complex in East Antarctica. Previously published work on this sample produced a near concordant Pb-loss age array spanning 400 million years despite showing a narrow range of $^{176}Hf/^{177}Hf_i$ values consistent with a single population of zircons. Zircons from the meta-gabbro are characterised by relative homogenous internal textures with no evidence of crystal plastic deformation nor significant radiation damage that would otherwise be consistent with diffusion related Pb-loss. In this study, in-situ laser-ablation inductively coupled plasma mass spectrometry (LA-ICP-MS) U—Pb isotope and trace element spot analyses in selected, representative grains from the meta-gabbro were combined with high-resolution backscatter electron imaging to link U—Pb isotopic and trace element variability to microstructures. Microstructures indicative of former coupled-dissolution precipitation replacement reactions such as abundant micro-scale porosity transgressing the interior of grains and sharp compositional reaction interfaces are common and are interpreted to be directly linked to enhanced trace element and U—Pb isotope mobility. Within each studied grain, several U—Pb analyses within a defined textural domain produced arrays of near-concordant dates spanning hundreds of millions of years between 500 Ma and 1000 Ma, where trace element concentrations are progressively depleted with increasingly younger dates. Our observations demonstrate that Pb-loss arrays, where only the oldest and youngest ages may be geologically significant, can result from variable trace element mobility and redistribution during melt-mediated coupled dissolution-precipitation replacement reactions within zircon.

1. Introduction

Zircon is an ideal geochronometer as it contains high concentrations of radioactive uranium and thorium, often contains negligible common lead (Hoskin and Schaltegger, 2003), can preserve important geochemical information even at extreme crustal conditions (Cherniak and Watson, 2001; Möller et al., 2003) and contains trace elements such as the rare earth elements, Y, Hf and Ti which can be used as important geochemical tracers (Belousova et al., 2002; Belousova et al., 2010; Cherniak and Watson, 2007).

Zircon U—Pb dating can produce two ideal endmember age patterns including: i) a well constrained gaussian distribution of concordant dates which is typically interpreted to represent crystallisation of a single population of zircons, and ii) an array of dates anchored at two points along the concordia curve where the upper intercept represents the age of the protolith, and the lower intercept reflects variable Pb-loss

* Corresponding author.
E-mail address: jean-antoine.gazi@hdr.mq.edu.au (J.-A. Gazi).

https://doi.org/10.1016/j.chemgeo.2026.123383
Received 21 September 2025; Received in revised form 18 March 2026; Accepted 22 March 2026
Available online 24 March 2026

during a defined geological event related to metamorphism or leaching of radiogenic Pb by weathering in radiation damaged zircon (Kramers et al., 2009). Depending on the age difference between upper and lower concordia intercepts, the data may form a discord or lie within error of the concordia, forming a near concordant Pb-loss array. The geological significance of a near concordant age array is therefore ambiguous because individual concordant dates may reflect partial disturbance of the U—Pb isotopic system or can be geologically meaningful.

Near concordant age arrays spreading over a hundred million years or more are common for zircon U—Pb geochronology from high temperature metamorphic terranes with complex structural and metamorphic histories (Clark et al., 2018; Korhonen et al., 2013; Laurent et al., 2018; Van Leeuwen et al., 2022). These age arrays are often interpreted as geological meaningful, in that they reflect continuous or episodic crystallisation and recrystallisation of zircon during prolonged high- and ultra-high-temperature metamorphism. Alternatively, near-concordant age arrays can be interpreted in the context of incomplete isotopic resetting during one or more short-lived geological events. Understanding the mechanisms facilitating Pb loss in zircons is therefore critical in evaluating the geological significance of each U—Pb date in the array, and by extension, the geological significance of the array itself.

Disturbance of the zircon U-Th-Pb isotopic system is understood in the context of diffusion and dissolution-precipitation processes. While volume-diffusion is sluggish in crystalline zircon (Cherniak and Watson, 2003; Möller et al., 2002), the accumulation of radiation damage over geological time can enhance the rates of Pb mobility in grains with sufficiently high concentrations of radioactive U and Th (Mezger and Krogstad, 1997). Cracking and interconnected amorphous domains associated with radiation damage can further enhance the mobility of geochemically important elements through fluid-mediated diffusion-reaction processes (Geisler et al., 2007). Microstructures such as dislocation arrays and dislocation movement caused by crystal-plastic deformation may also result in enhanced rates of U, Th and Pb mobility through pipe diffusion (Piazolo et al., 2012; Piazolo et al., 2016; Reddy et al., 2006; Timms et al., 2006).

Disturbance of the U-Th-Pb isotopic system through radiation damage and crystal plastic deformation cannot account for incomplete isotopic resetting in grains which experienced little strain, have low concentrations of U and Th and/or had insufficient time to accumulate enough radiation damage to significantly disrupt the crystal lattice. In these cases, isotopic disturbance may be facilitated by dissolution-precipitation processes (Martin et al., 2008; Rubatto and Hermann, 2003; Tomaschek et al., 2003). When dissolution and precipitation are closely coupled in space and time (pseudo-morphic replacement reactions after Putnis, 2009), variable redistribution of radiogenic Pb within the precursor grain and Pb-loss may lead to spurious age patterns as demonstrated in natural (Condit et al., 2018; Daczko et al., 2024; Halpin et al., 2020; Martin et al., 2008; Rubatto et al., 2008; Seydoux-Guillaume et al., 2015; Skrzypek et al., 2020; Soman et al., 2010; Spier et al., 2022; Weinberg et al., 2020) and experimental studies (Asimus et al., 2024; Grand'Homme et al., 2016; Spruzeniece et al., 2017a; Varga et al., 2020). Analysing zircon domains where original zircon has been replaced by coupled dissolution-precipitation (CDP) after its initial crystallisation may generate geologically meaningless ages for the zircon grain, and by extension the rock sample hosting these grains. Rim domains formed by zircon CDP replacement should be carefully distinguished from situations when dissolution and precipitation are spatially and temporally decoupled, as in the case of a rim overgrowth. In the latter case, the measured U—Pb date is interpreted as geologically meaningful.

Although the role of hydrothermal and aqueous fluids in CDP replacement reactions have been well-established in experimental and natural studies, recent studies have increasingly recognised the importance of melt in the crystallisation and reaction history of high-grade metamorphic rocks that have experienced incipient partial melting or melt migration through pervasive (Stuart et al., 2016) and discrete porous melt flow (Daczko et al., 2024; Meek et al., 2019). Despite increasing recognition, microstructures indicative of the former presence of melt can be easily overlooked, especially when the composition of externally derived melts is similar to the bulk composition of the host rock (Stuart et al., 2016). Melt-mediated CDP reactions also extend to igneous systems, where magmas can be contaminated with foreign crystals (inherited or xenocrystic zircon) that did not form in situ from their host magma i.e., grains entrained during melt generation, ascent and emplacement (Miller et al., 2007; Paterson et al., 1992). In the case of Zr-undersaturated magmas, the entire zircon population may be inherited and modified by the host magma (Halpin et al., 2020). Despite the broad range of geological environments in which zircon-melt interactions can occur, the effect of melt-mediated CDP reactions on the geochronology of important U-bearing minerals like monazite and zircon is only rarely recognised and poorly understood (Daczko et al., 2024; Spier et al., 2024; Spier et al., 2022).

To assess the underlying processes related to near concordant age arrays spreading over a hundred million years, we re-examine in detail the U—Pb isotope systematics and microchemistry of three select zircon grains from a meta-gabbro within the Mawson Charnockite composite pluton from East Antarctica previously published by Halpin et al. (2012). The chosen suite of zircons is ideally suited for our study, as the Halpin et al. (2012) study dated 56 zircons (one spot per zircon) producing a near concordant array of U—Pb dates spanning 400 million years despite exhibiting a narrow range of $^{176}Hf/^{177}Hf_i$ values consistent with crystallisation of a single age population of zircon from a parental magma. In this study, we combine high-resolution backscatter electron (BSE) and cathodoluminescence (CL) imaging with multiple spot analyses (up to 7 spots per grain) to link isotopic and trace element chemical variability to microstructures within zircon grains. The aim of our study is to improve the understanding of processes involved in redistributing radiogenic Pb to form near-concordant U—Pb age arrays by linking chemical and microstructural signatures to processes. Our results show that melt-mediated CDP both redistributes trace elements within individual grains and causes intra-grain Pb mobilization and variable Pb loss, producing complex, heterogenous U—Pb age distributions within single zircon crystals. Accordingly, we interpret the extensive, near concordant zircon U—Pb age array in the Macklin Island meta-gabbro as the product of melt-mediated CDP reactions.

2. Geological overview

Early geological mapping of the Mawson coast in East Antarctica distinguished two main groups of rocks including an aerially extensive orthopyroxene bearing orthogneiss body, the Mawson Charnockite, and the older paragneisses and felsic orthogneisses which it intruded (Crohn, 1959; Trail, 1970). These rocks form part of a larger Meso-Neoproterozoic mobile belt extending from western Enderby Land to the northern Prince Charles Mountains known as the Rayner Complex (Fig. 1a). The Rayner Complex, along with contiguous rocks found in the Eastern Ghats granulite belt in India, record extensive melting and deformation during a 1000 Ma – 900 Ma collision between a part of East Antarctica with proto-India (Dunkley et al., 2002; Halpin et al., 2005; Halpin et al., 2007; Kelly et al., 2004; White and Clarke, 1993), either as part of the Rodinia supercontinent (Li et al., 2008) or as an isolated continent (Merdith et al., 2017). Australo-Antarctic and Indo-Antarctic provinces were finally assembled within Gondwana between c. 650 Ma and 500 Ma, in what is typical referred to as the Kuunga Orogen (Boger, 2011; Daczko and Halpin, 2025; Daczko et al., 2018; Fitzsimons, 2000; Mulder et al., 2019). Deformation, metamorphism and melting related to this assembly is found throughout East Antarctica (Boger et al., 2002; Liu et al., 2006; Liudong et al., 2018; Mikhalsky and Kamenev, 2013; Van Leeuwen et al., 2019; Zhao et al., 2003), but has yet to be identified along the Mawson Coast including within the Mawson Charnockite.

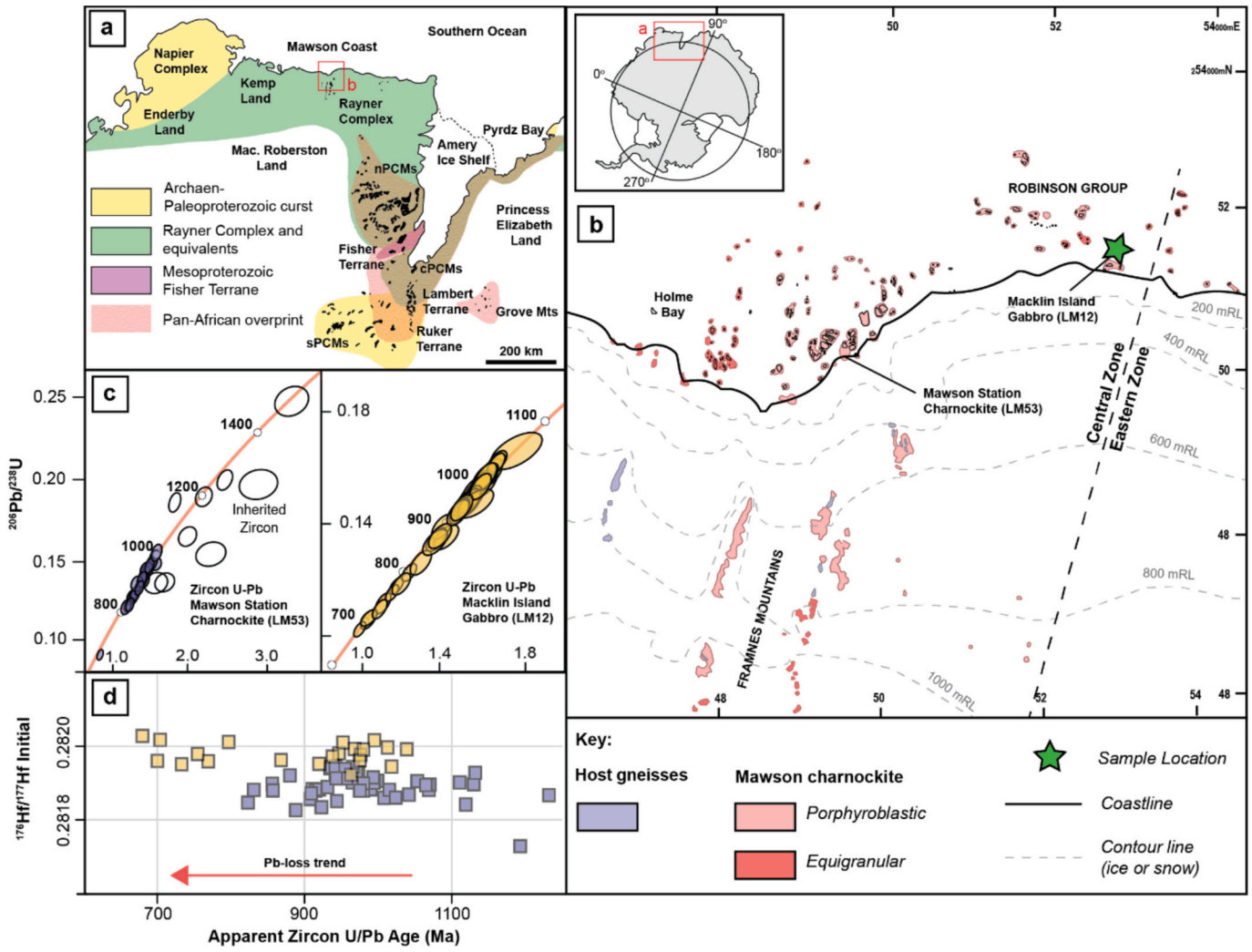

Fig. 1. (a) Simplified geological map of East Antarctica showing the Proterozoic Rayner Complex and surrounding tectonic terranes with the Mawson coast 1:250000 geological map area highlighted in (b), modified after Phillips et al. (2009). (b) 1:250000 geological map of Mawson and Mount Henderson (Australia. Bureau of Mineral Resources, G., Geophysics, 1967) with the location of the Macklin Island gabbroic gneiss (LM12) and Mawson Station charnockite (LM53) shown. (c) U—Pb geochronology of sample LM12 and LM53 showing near concordant age arrays (Halpin et al., 2012). (d) Summary of Hf isotope data from Halpin et al. (2012) showing a narrow range of Hf isotope values for the Macklin Island meta-gabbro and Mawson Station charnockite suggesting zircons crystallised from a common parental magma. The horizontal shift in initial Hf values is indicative of Pb-loss.

The Mawson Charnockite as defined by Trail (1970) is a ~ 3000 km^2 composite pluton dominated by foliated, medium grained to coarse grained, plagioclase-quartz-orthopyroxene granitoids mapped as either equigranular or porphyroblastic occurrences (Fig. 1b) (Crohn, 1959; Trail, 1970; Young and Ellis, 1991; Young et al., 1997). The rocks comprising the Mawson Charnockite typically have intermediate compositions from quartz monzodiorite through to granodiorite and quartz monzonite with rare occurrences of mafic compositions including the Macklin Island meta-gabbro, sampled from the Robinson Group islands (Fig. 1b) (Crohn, 1959; Trail, 1970; Young and Ellis, 1991). Mafic rocks within the Mawson Charnockite occur as discordant dykes or as concordant, metre thick lenses with essentially the same mineral assemblage as the surrounding charnockite (Trail, 1970), with the later example being the most likely setting of the Macklin Island meta-gabbro. Like other charnockites mapped in East Antarctica, the Mawson Charnockite is considered to be derived by high temperature partial melting of granulitic lower crustal sources (Young et al., 1997). High crystallisation temperatures are supported by feldspar thermometry, the observation of partially melted gneissic xenoliths, and rare exsolved pyroxenes (Young and Ellis, 1991).

Based on zircon U—Pb dating and field relationships, intrusion of the Mawson Charnockite was interpreted to have occurred during or soon after the peak of ca. 1000 Ma Rayner Orogen metamorphism (Young and Ellis, 1991; Young and Black, 1991). Intrusive contacts between charnockites and the host gneisses cut two episodes of deformation (D1–D2) (Crohn, 1959; Young and Ellis, 1991). Two phases of deformation (D3–D4) that post-date emplacement of the Mawson Charnockite resulted in the formation of tight to open, upright folding and partial recrystallisation of the charnockites with new garnet, hornblende and biotite formed in many rocks (Crohn, 1959; Young and Ellis, 1991). D3 deformation occurred around ~920 Ma whilst D4 deformation occurred at approximately 910 Ma based on *syn*-D4 intrusive rocks found around Cape Bruce, to the west of the Mawson Coast (Dunkley et al., 2002). Metapelitic gneisses from Cape Bruce and Forbes Glacier indicate an anticlockwise P-T-t path during D1–D4 between ca. 990–910 Ma with peak temperatures between 850 °C–900 °C and peak pressures between 5 and 6 kbar (Halpin et al., 2007).

3. Historic geochronology of the Mawson Charnockite

Early workers using zircon ion-microprobe U—Pb dating obtained weighted average $^{207}Pb/^{206}Pb$ ages of 985 ± 29 Ma (19/21 analyses)

and 954 ± 12 Ma (20/21 analyses) selecting only near-euhedral zircons under the assumption that the zircon populations within the charnockite samples reflected a single igneous population (Young and Black, 1991). In a Wetherill concordia diagram, dates from the Young and Black (1991) study appear mostly concordant or near concordant and are spread between 1050 Ma and 850 Ma highlighting some complexity within the data with the authors noting that this scatter could be attributed to random error or slight isotopic disturbance. Given the overall igneous character of zircons recovered from the charnockites, the weighted $^{207}Pb/^{206}Pb$ ages were interpreted by the authors to date the emplacement of the plutonic complex. Younger Rb—Sr whole rock dates of 886 ± 48 Ma and 910 ± 18 Ma from the charnockites were then re-interpreted to date resetting of the Rb—Sr system during the Rayner Structural Episode (Young and Black, 1991).

More recent attempts at zircon U—Pb dating further highlighted complexity in zircon U—Pb data with samples producing an array of near concordant dates between 1100 Ma and 680 Ma (Fig. 1c) (Halpin et al., 2012). Despite the spread of U—Pb dates in each sample, the intra-sample $^{176}Hf/^{177}Hf_i$ values are clustered (Fig. 1d) leading those authors to interpret the age arrays as Pb-loss arrays and that the zircons likely crystallised from a single parental magma. BSE and CL imaging of zircons show complex core-rim structures, extensive cracking and abundant inclusions made up by minerals including monazite, apatite, biotite, quartz, feldspars, pyroxenes, and rutile (Fig. 2). Electron Backscatter Diffraction (EBSD) analyses of two representative zircons showed limited evidence of radiation damage or crystal plastic deformation (suppl. Material 5; Halpin et al., 2012). Thus, Pb remobilisation due to radiation damage or pipe diffusion along sub-grain boundaries related to crystal plastic deformation could be ruled out as processes responsible for the observed complex geochronological pattern. Halpin et al. (2012) interpreted the U—Pb age arrays to be the result of partial lead-loss facilitated by Pb mobility during the high-temperature, high-strain Rayner Structural Episode followed by recent Pb-loss enabled by metamictisation and cracking. In their approach, a minimum crystallisation age was determined using the oldest concordant U—Pb date in the array. Instead of a single crystallisation age, the plutonic complex was suggested to have been emplaced episodically at 1145–1140 Ma, 1080–1050 Ma and 980–965 Ma (Halpin et al., 2012). In the case of the Macklin Island meta-gabbro, U—Pb dates produced a near concordant array between 1100 Ma and 680 Ma (Fig. 1c) with a minimum crystallisation age based on the oldest $^{207}Pb/^{206}Pb$ spot age of 1049 ± 39 Ma.

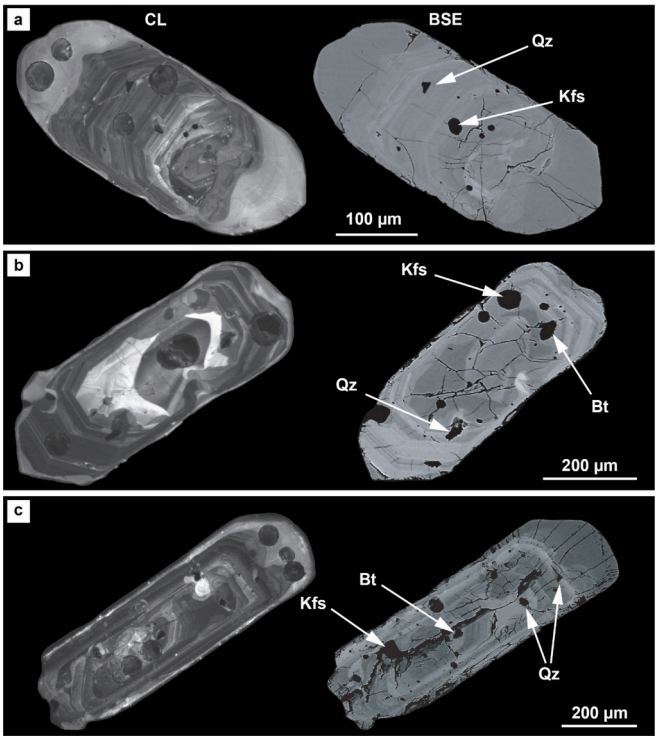

Fig. 2. Representative Cathodoluminescence (CL) and back-scattered electron (BSE) images of zircon grains from the Mawson Charnockite published by Halpin et al. (2012). Back-scatter electron images show abundant micron to sub-micron scale inclusions with spherical or irregular shapes. The inclusions are monomineralic and polymineralic, comprising minerals such as Bt, Qz, Kfs, Pl, Ap and Mnz. CL images show very similar features as BSE images suggesting compositional rather than structural changes are shown by CL signal. Note round variable grey spots highlighted by thin stippled white lines in CL images signify spots of analyses. Mineral abbreviations after Whitney and Evans (2010).

4. Analytical methods

4.1. Petrography

A cover-slipped thin (30 µm) section of the Macklin Island meta-gabbro (sample LM12 in the Halpin et al. (2012) study) was provided by the University of Tasmania (UTAS). The petrographic description of the thin section was made using a Nikon Eclipse 50i optical microscope. Mineral abbreviations follow the scheme proposed by Whitney and Evans (2010).

4.2. Zircon imaging

Zircon grains from the Macklin Island meta-gabbro including grains LM12-4-29, LM12-5-24, and LM12-5-10 from the Halpin et al. (2012) study were provided by the University of Tasmania (UTAS) in a polished, epoxy resin grain mount for use in this study. In this study, grains LM12-5-10, LM12-5-24, and LM12-4-29 will be referred to as grains 1, 2 and 3, respectively. Prior to U—Pb and trace element characterisation of zircon grains by LA-ICPMS, cathodoluminescence and high-resolution BSE images were obtained using the Zeiss BSD detector and Zeiss CL detector on the Zeiss EVO-MA 15 SEM at MQ GeoAnalytical (MQGA), Macquarie University. The SEM was operated under high vacuum at an accelerating voltage of 15 kV and working distance of 12 mm.

In addition, 20 newly handpicked zircon grains from a LM12 heavy mineral separate provided by UTAS were mounted on a stub using double sided carbon tape for whole grain imaging. Whole grain BSE images were obtained using the PHENOM XL benchtop SEM at the Macquarie University Microscopy Unit. The PHENOM XL SEM was operated under high vacuum using an accelerating voltage of 10 kV and working distance of 6.8 mm.

4.3. U—Pb dating and trace-element analysis

The U—Pb and trace element compositions of zircons were characterised using an Agilent 7700cx quadrupole ICPMS instrument, attached to a Photon Machines Excimer 193 nm laser ablation system with HelEx at MQGA, Macquarie University. Zircons were analysed using a 50 µm laser beam size with a firing frequency of 5 Hz and a beam energy density of 7 J/cm^2. U—Pb isotopes (^{206}Pb, ^{207}Pb, ^{204}Pb, ^{232}Th, ^{238}U and ^{235}U) and trace elements (^{28}Si, 29Si, ^{31}P, ^{43}Ca, ^{49}Ti, ^{89}Y, ^{90}Zr, ^{92}Zr, ^{93}Nb, ^{139}La, ^{140}Ce, ^{141}Pr, ^{146}Nd, ^{147}Sm, ^{151}Eu, ^{157}Gd, ^{159}Tb, ^{163}Dy, ^{165}Ho, ^{166}Er, ^{169}Tm, ^{173}Yb, ^{175}Lu, ^{177}Hf, ^{178}Hf, ^{181}Ta) were obtained simultaneously. Each analysis began with a 60 s blank gas measurement followed by a further 120 s of analysis time during ablation. A typical run contained 8 to 12 analyses of an unknown sample bracketed by two analyses of standard reference materials including the NIST-610 glass for trace elements and GJ-1 zircon for U—Pb isotopes. Additionally, analyses of the standard basalt glass, BCR2-G, and zircon standards 91,500 and Mudtank were used as secondary reference materials throughout the duration of the study to provide an independent control to assess accuracy, precision and instrument stability. Measured U—Pb

ages for Mudtank and 91,500 in this study (see supplementary 1) agree with the previously published ages determined by LA-ICPMS of 733 ± 27 Ma and 1061 ± 36 Ma respectively (Jackson et al., 2004). Trace element concentrations of BCR2-G and GJ-1 zircon reported in this study agree with reference values within 1–2% for rare earth elements (REE), Y, Nb, Ta, Th and U at the ppm level.

U—Pb ages and trace element concentrations were calculated from raw signal data using the software package GLITTER (Griffin, 2008). Representative ages for each analysis were obtained by selecting the flattest part of the 120 s signal. U—Pb isotope data are presented in concordia diagrams made using IsoplotR (Vermeesch, 2018) and age uncertainties in this paper are reported as 2σ uncertainties. Trace element concentrations were obtained using ^{90}Zr as an internal standard and NIST-610 glass for external calibration.

Total REE concentrations, reported in Fig. 6, are calculated by summation of measured REE including ^{139}La, ^{140}Ce, ^{141}Pr, ^{146}Nd, ^{147}Sm, ^{151}Eu, ^{157}Gd, ^{159}Tb, ^{163}Dy, ^{165}Ho, ^{166}Er, ^{169}Tm, ^{173}Yb, and ^{175}Lu.

4.4. Theoretically determined degree of radiation damage

Theoretical alpha decay doses are calculated following the procedure described by Nasdala et al. (2001) using U and Th concentrations measured by LA-ICPMS for a duration of 1000 million years and 500 million years. These durations reflect two scenarios discussed by Halpin et al. (2012) whereby (i) the charnockites remained at mid-crustal levels until at least 500 Ma where the P-T conditions >500 Ma promoted recovery of radiation damage, or (ii) the charnockites were exhumed to the upper crust shortly after emplacement and accumulated radiation

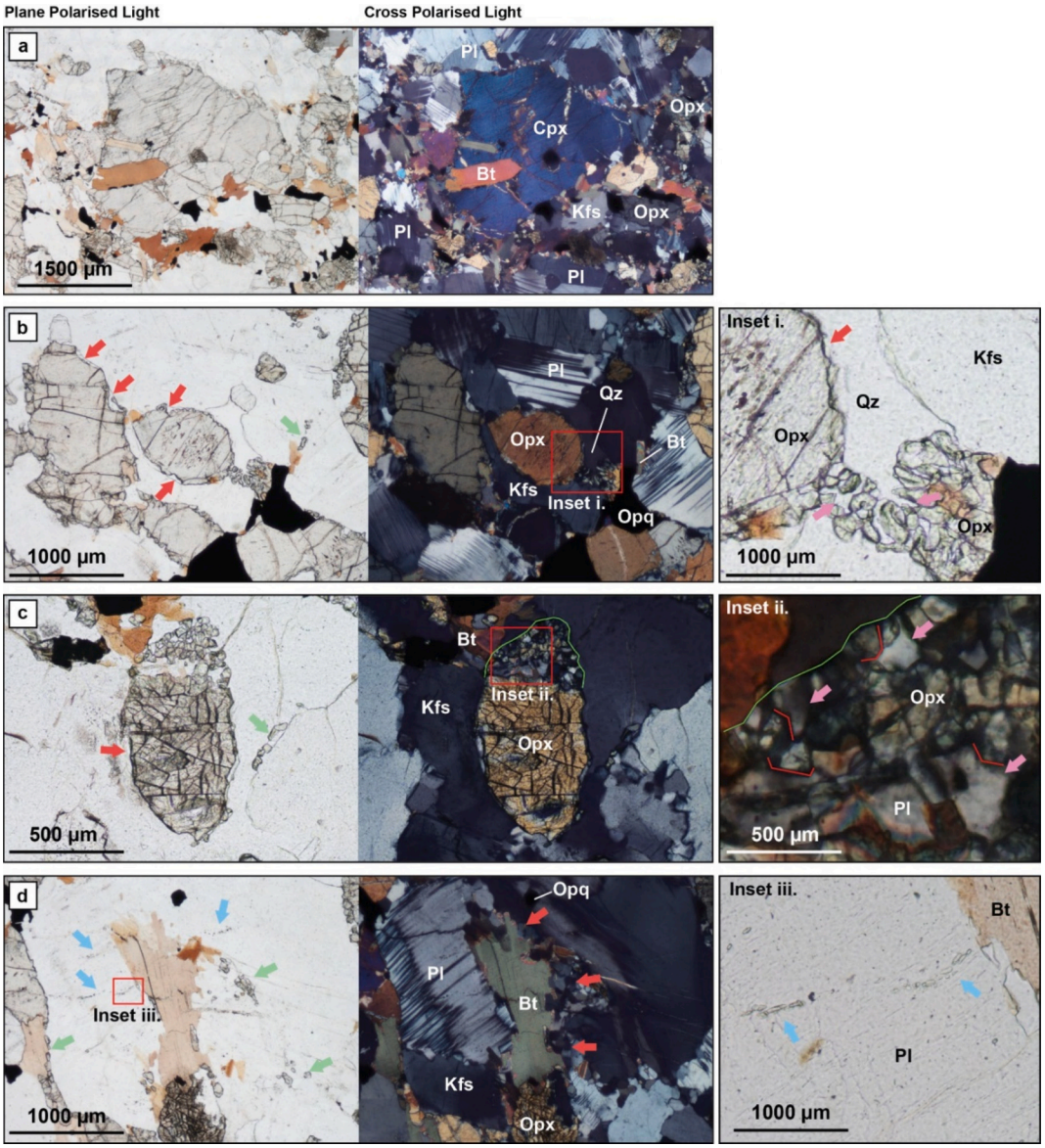

Fig. 3. Plane (PPL) and cross polarised (XPL) photomicrographs highlighting the main microstructural characteristics of the Macklin Island meta-gabbro. (a) a large equant Cpx grain showing non-uniform extinction and partial replacement by Bt. (b) Opx grains with cuspate, corroded grain boundaries infilled with elongate feldspar or quartz grains (red arrows) and fine grained, recrystallised grains along grain boundaries. Fine-grained Opx are observed in 'string of beads' type textures (green arrows). Quartz grain infilling interstices of corroded Opx grain, pink arrows Inset i (c) Opx grain partially replaced by fine-grained Opx, Pl, and Kfs (replaced area outlined by green line). Inset ii. shows fine-grained Opx + Pl partially replacing a larger Opx grain. Straight crystal faces are highlighted by red lines and similar extinction angles in interstitial feldspars by pink arrows. (d) Coarse grained Bt replaced by fine-grained Bt and Pl/Kfs (red arrow). Adjacent feldspar grains transgressed by inclusion trails (blue arrows in Inset iii.). (For interpretation of the references to colour in this figure legend, the reader is referred to the web version of this article.)

damage for 1000 million years. Calculated alpha decay doses represent the maximum possible accumulation of alpha-decay events as zircon recovery (healing of radiation damage) can occur through several mechanisms over a wide temperature range between 150 °C and 1000 °C (Ginster et al., 2019).

5. Results

5.1. Petrographic features of the Macklin Island meta-gabbro

The Macklin Island meta-gabbro comprises plagioclase (45–55 vol %), orthopyroxene and clinopyroxene (30–40 vol% in approximately equal proportions), orthoclase (5–10 vol%), biotite (5–10 vol%) with minor quartz and accessory minerals including zircon, apatite, and opaque grains. Coarse grained plagioclase, pyroxene, orthoclase, and biotite show microstructural evidence of minor internal deformation such as undulose extinction (Fig. 3a), deformation twinning (Fig. 3b), kink bands and sub-grains (Fig. 3c, d). Plagioclase and orthoclase grain boundaries appear sutured to irregular (Fig. 3) with rare straight boundaries between adjacent feldspar grains or pyroxene grains (Fig. 3a). Coarse grained plagioclase, orthoclase and pyroxenes can also have a 'dusty' appearance resulting from a high density of micron-scale inclusions (blue arrows, Fig. 3d, Inset iii.). The distribution of micro-inclusions in these minerals is spatially related to the presence of biotite at the grain margins. Pyroxene grains are equant or exhibit irregular 'strung out' grain shapes with recrystallised and corroded grain margins (Fig. 3a, b). Cuspate pyroxene grains have grain boundaries lined by small, elongate grains of feldspar, quartz, or biotite grains (red arrows, Fig. 3b). Opaque grains (typically <0.3 mm) tend to be spatially associated with biotite and are almost always xenomorphic, filling the interstices between adjacent pyroxene and feldspar grains (Fig. 3a, b). Coarse grained biotite (0.3–0.8 mm) can share straight boundaries between plagioclase and pyroxene whilst cuspate boundaries are typically observed between biotite and opaque grains.

Fine grained aggregates of feldspars, biotite and pyroxene are observed as i) equant grain aggregates infilling embayments along grain boundaries of coarse-grained plagioclase feldspar, orthoclase feldspar, pyroxene, and biotite (Fig. 3b, d), ii) as partial replacement of pyroxene grains (Fig. 3c), iii) along grain boundaries between the major mineral phases (Fig. 3d) and iv) surrounding 'islands' of optically continuous plagioclase or pyroxene grains. Additionally, fine-grained pyroxene can also be observed forming 'string of beads' type textures (green arrows, Fig. 3b–d). Plagioclase in fine-grained aggregate textures often appear xenomorphic with small dihedral angles at pyroxene-pyroxene junctions or have polygonal grain boundaries whilst fine-grained pyroxene tends to display straight crystal faces (Fig. 3c).

5.2. Zircon imaging

Back-scattered electron (BSE) images of whole zircons grains picked from the LM12 heavy mineral separate have elongate, doubly terminating morphologies when not fractured (Fig. 4b, c, d). Grain edges

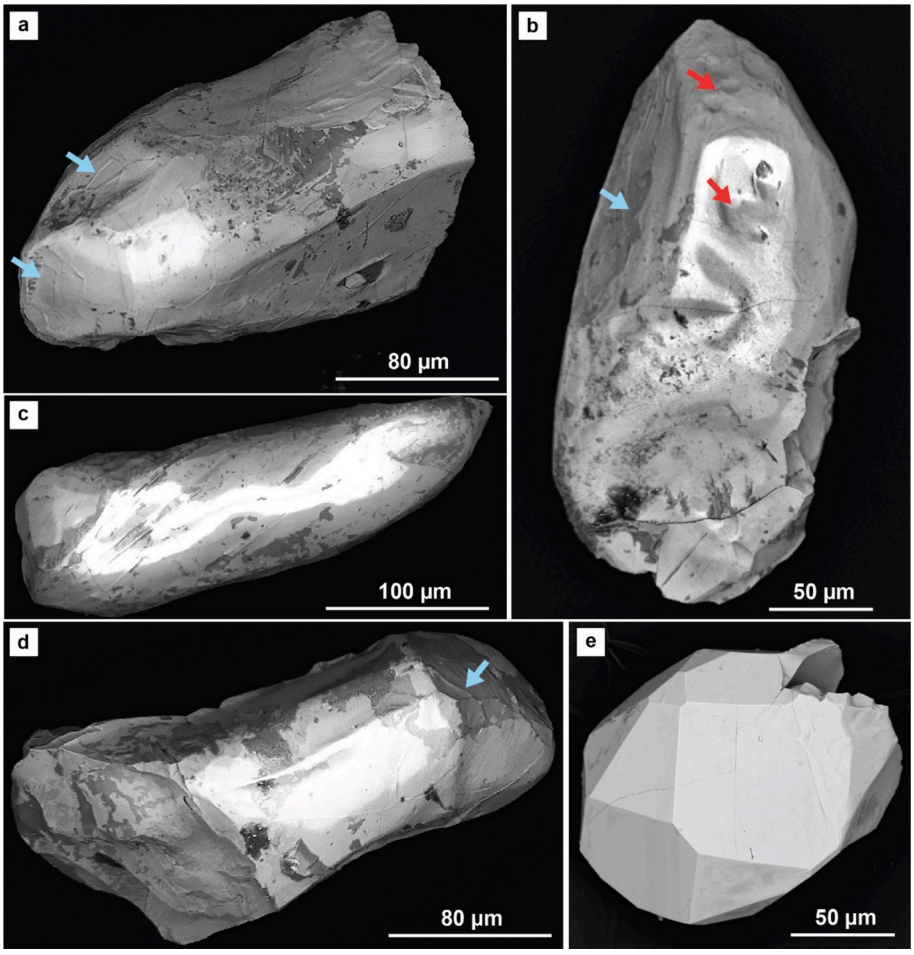

Fig. 4. BSE images showing the surface features of non-polished, whole zircon grains from the Macklin Island meta-gabbro (a–d) with a zircon from the Temora gabbroic diorite which is used as a U—Pb standard reference material for comparison (e); note the contrast between the studied and reference material. Red arrows highlight dissolution pitting and blue arrows highlight dissolution related 'honeycomb' surface textures. (For interpretation of the references to colour in this figure legend, the reader is referred to the web version of this article.)

appear curvilinear and embayed with all grains exhibiting rounded to sub-angular crystal terminations (Fig. 4a–d). The surface of these grains is characterised by the appearance of distinct 'honeycomb' textures (blue arrows in Fig. 4a, b, d) and dissolution pitting (red arrows in Fig. 4b). For reference, a zircon grain from the Temora gabbroic diorite, used as a standard reference material for U—Pb geochronology is shown; it displays euhedral crystal faces and straight grain boundaries (Fig. 4e).

High resolution BSE and cathodoluminescence (CL) images from three representative grains from the Macklin Island meta-gabbro are shown in Fig. 5. The three grains range in size from 600 μm to 750 μm in length, have elongate, prismatic morphologies with sub-rounded to sub-angular terminations and exhibit minor cracking (Fig. 5). All three grains have CL-dark interiors and a thin, faintly zoned to unzoned CL-bright rim less than 20 μm thick with linear to curvilinear inward penetrating, lobate boundaries (Fig. 5b, d, f). CL-bright domains are also observed within the interior of grain 1 as discrete ovoid features (Fig. 5b) and transecting the lower portion of grain 2 in fracture-like bands (Fig. 5d). Large portions of the CL-dark core in each grain have a homogenous CL response, or in the case of grain 3, the entire core appears homogenous (Fig. 5f). In grains 1 and 2, blurry oscillatory

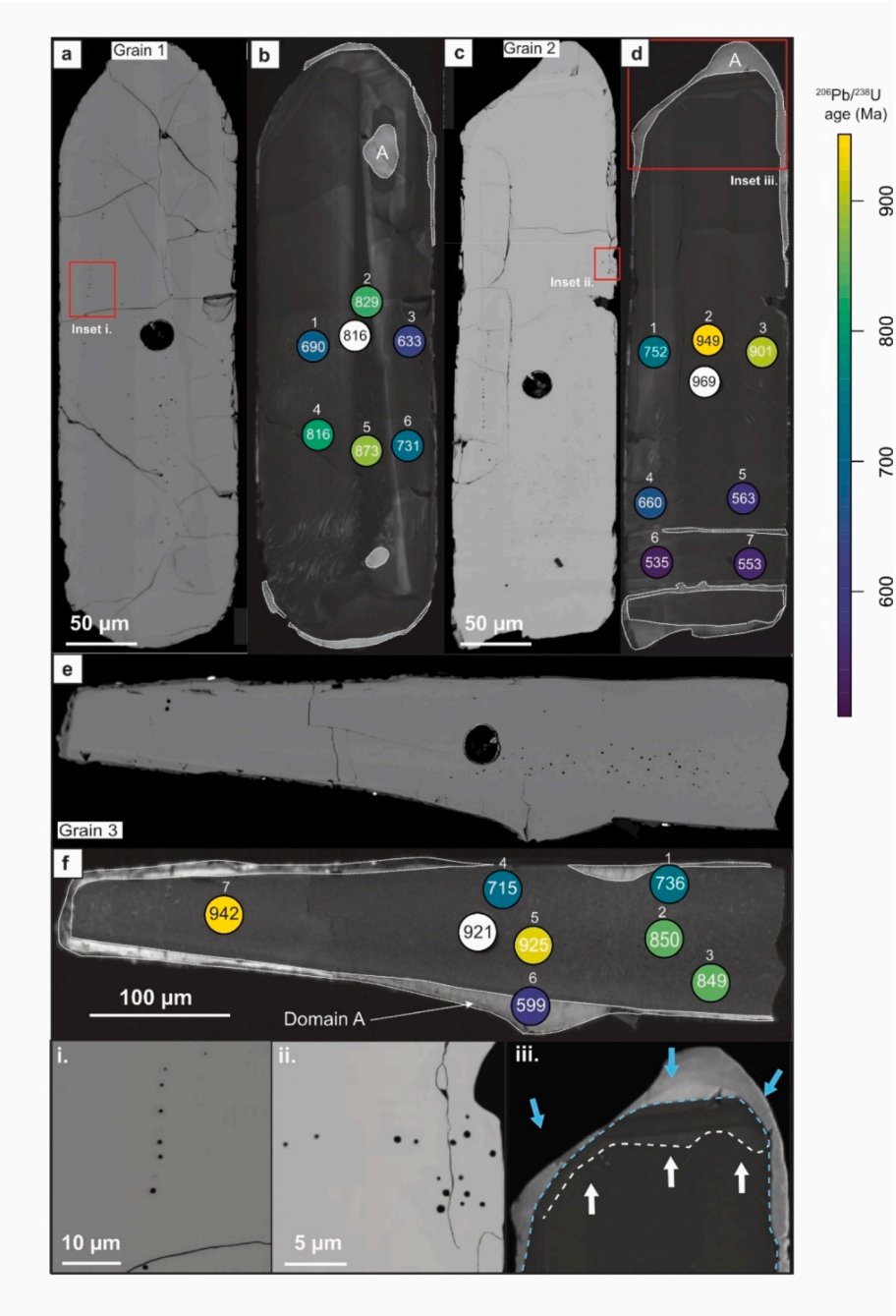

Fig. 5. CL and BSE images of zircon grains 1 (a–b), 2 (c–d) and 3(e–f) showing internal microstructures and CL domains (Domain A outlined in white dashed lines). Porosity is observed as trails (Inset i.), clusters (Inset ii.) or dispersed throughout the grain. In grain 2, remnant oscillatory zoning is cut by the CL-dark, homogenous interior (dashed white line) and by the CL-bright ('bleached) rim (dashed blue line) (Inset iii.). White and blue arrows indicate the apparent direction of the reaction progression. LA-ICPMS spot locations shown and coloured according to the measured apparent $^{206}Pb/^{238}U$ ages. White circles indicate LA-ICPMS spots from Halpin et al. (2012). Average 2σ uncertainty for apparent $^{206}Pb/^{238}U$ ages is 18 Ma. (For interpretation of the references to colour in this figure legend, the reader is referred to the web version of this article.)

zoning is confined to narrow regions adjacent to the CL-bright rims (Fig. 5d, f) and in grain 2, the CL-dark homogenous core domain cuts blurry oscillatory zoning preserved adjacent to the CL-bright rim (Fig. 5d and Inset iii.). Abundant micro- to submicron scale porosity (5 μm to <1 μm diameter) is observed in each grain as i) linear trails within the interior of the grain that can be concordant with CL zoning, or discordant, cutting across CL features (Fig. 5a, c, e and Inset i) and ii) dispersed through parts of a grain as clusters (Fig. 5e, Inset ii). Although rare, visible porosity is also observed in some areas of the CL-bright rims (Fig. 5c, inset ii).

5.3. Zircon U—Pb geochronology and microchemistry

For each grain, several locations within the CL-dark core were targeted for U—Pb and trace element laser ablation ICP-MS analysis, Figs. 6 and 7 (full dataset provided in Supplementary Table 1 and 2). Overall, measured U—Pb ages for each grain form a concordant array of ages from 950 Ma to 650 Ma. In comparison, measured Th—Pb ages (Fig. 8) show a systematic shift toward older ages and reverse discordance.

In grain 1, six analyses produced an array of concordant and near concordant U—Pb dates ranging from 633 ± 12 Ma to 873 ± 20 Ma (Fig. 6a, b). The oldest $^{206}Pb/^{238}U$ date of 873 ± 20 Ma was located within a dark, porous CL band in the interior of the grain whilst the youngest measured $^{206}Pb/^{238}U$ date of 633 ± 12 Ma was obtained toward the edge of the grain where porosity is absent, and the CL response is uniform (Fig. 5d). Measured U (243 ppm to 909 ppm) and Th (147 ppm to 917 ppm) concentrations are variable and tend to decrease with younger $^{206}Pb/^{238}U$ dates (Fig. 7a). Thorium–uranium ratios for four analyses were > 1.25 whilst two analyses near the edge of the grain (Spot 3 and Spot 6) had significantly lower Th/U values of 0.30 and 0.28; these spots also had the lowest measured Th concentrations (<250 ppm), but similar U concentrations compared to the four spots located within the interior of the grain (Fig. 7b). Rare earth element (REE) patterns for five analyses are similar, showing strong enrichment of heavy REE (HREE) over light REE (LREE) with a strong positive Ce anomaly and strong negative Eu anomaly (Fig. 7c). Spot 2, located over porosity, showed enrichment of LREE. Total REE (257 ppm to 940 ppm), Yttrium (352 ppm to 1478 ppm) and Phosphorus (174 ppm to 394 ppm) concentrations are variable across the grain with Yttrium and REE concentrations progressively decreasing with younger $^{206}Pb/^{238}U$ dates

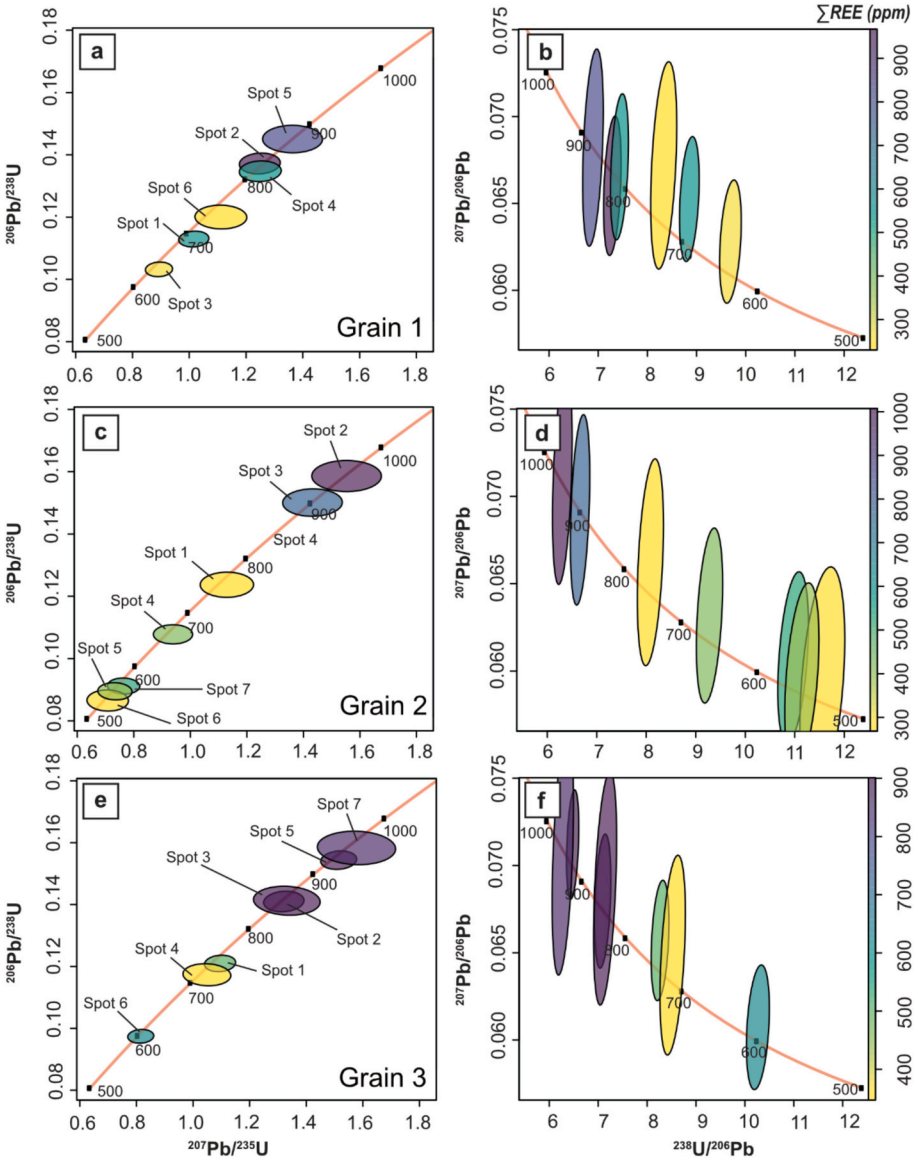

Fig. 6. Zircon U—Pb Wetherill and Terra-Wasserberg Concordia diagrams for grain 1 (a–b), grain 2 (c–d), and grain 3 (e–f). U—Pb age ellipses are coloured according to their total REE concentrations.

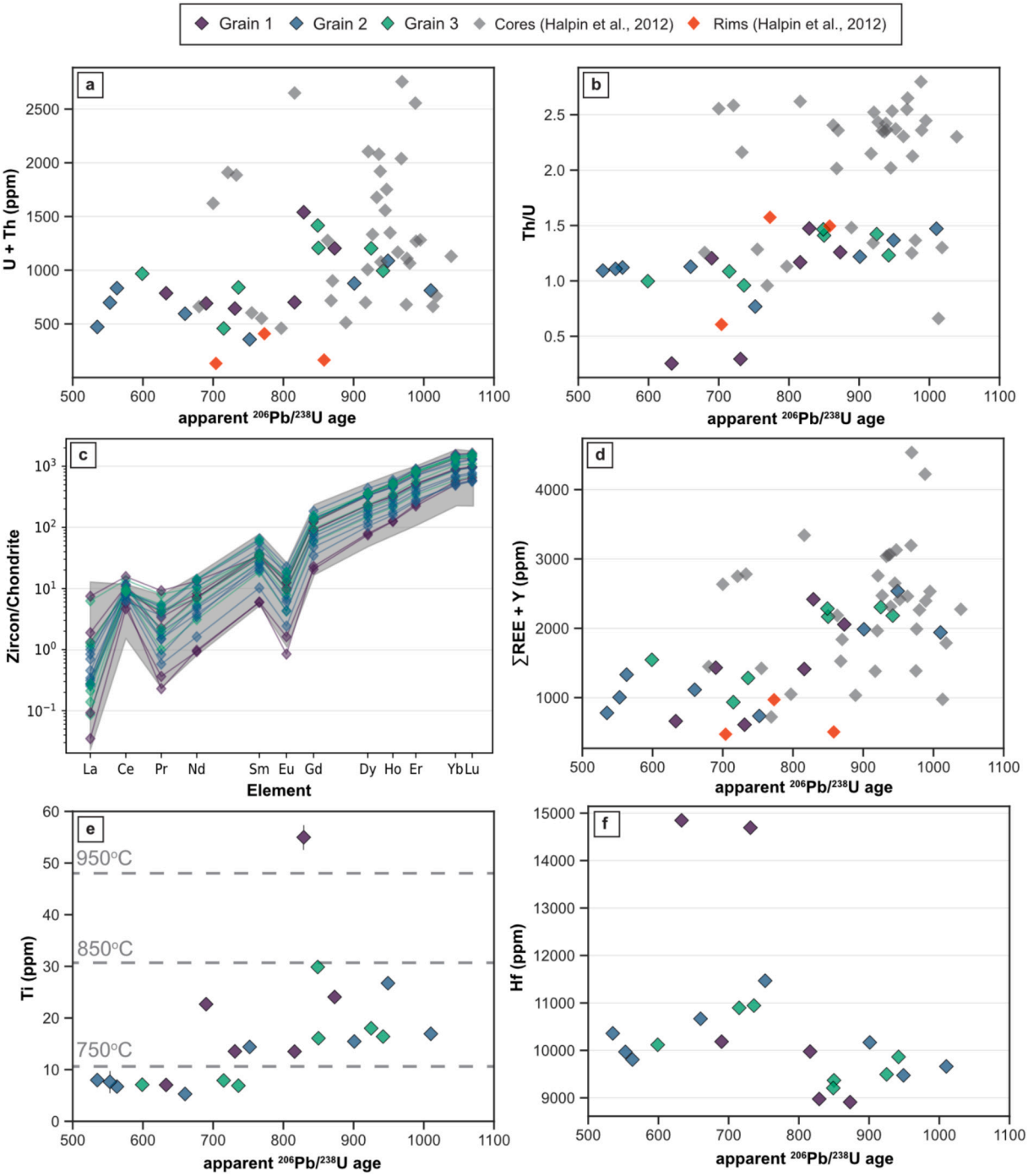

Fig. 7. Trace element compositional variations in zircon from grain 1, grain 2 and grain 3 with available zircon trace element data from LM12 published by Halpin et al. (2012) plotted for reference (grey markers). Grey dashed lines in (e) represent estimated temperatures calculated using the Ti-in-zircon thermometer (Ferry and Watson, 2007) assuming aTiO2 = 0.75 and aSiO2 = 1. Average 2σ uncertainty for apparent $^{206}Pb/^{238}U$ ages is 18 Ma. If not shown, error bars for trace element data points are smaller than the symbol.

(Fig. 7d). Hafnium concentrations (8910 ppm to 14,848 ppm) are variable across the grain with higher concentrations generally correlating with younger $^{206}Pb/^{238}U$ dates. The two anomalously high Hf concentrations (>1400 ppm) were recorded in Spot 3 and Spot 6 at the edge of the grain. The highest Ti concentration of 55 ppm was measured on Spot 2 which had a $^{206}Pb/^{238}U$ date of 829 ± 16 Ma, and the lowest Ti concentration of 7 ppm was measured on Spot 6. Although there is a general trend of progressive decreases in Ti concentrations with younger measured dates, spot 1 ($^{206}Pb/^{238}U$ date of 690 ± 12 Ma) showed a similar Ti concentration of 23 ppm when compared to spot 5 ($^{206}Pb/^{238}U$ date 873 ± 20 Ma, Ti = 24 ppm).

In grain 2, seven analyses produced an array of concordant dates ranging from 949 ± 22 Ma to 535 ± 16 Ma (Fig. 6c, d). The oldest $^{206}Pb/^{238}U$ date of 949 ± 22 Ma (Spot 2) came from the centre of the grain where the CL response was homogenous, and no porosity or cracking is observed (Fig. 5f). The four youngest $^{206}Pb/^{238}U$ dates range from 660 ± 14 Ma to 535 ± 16 Ma and were obtained from the bottom half of the grain (Spots 4 to 7) where the CL response is mostly homogenous with some faint planar banding and dispersed nano- to micron-scale porosity (Fig. 5f). Uranium concentrations (243 ppm to

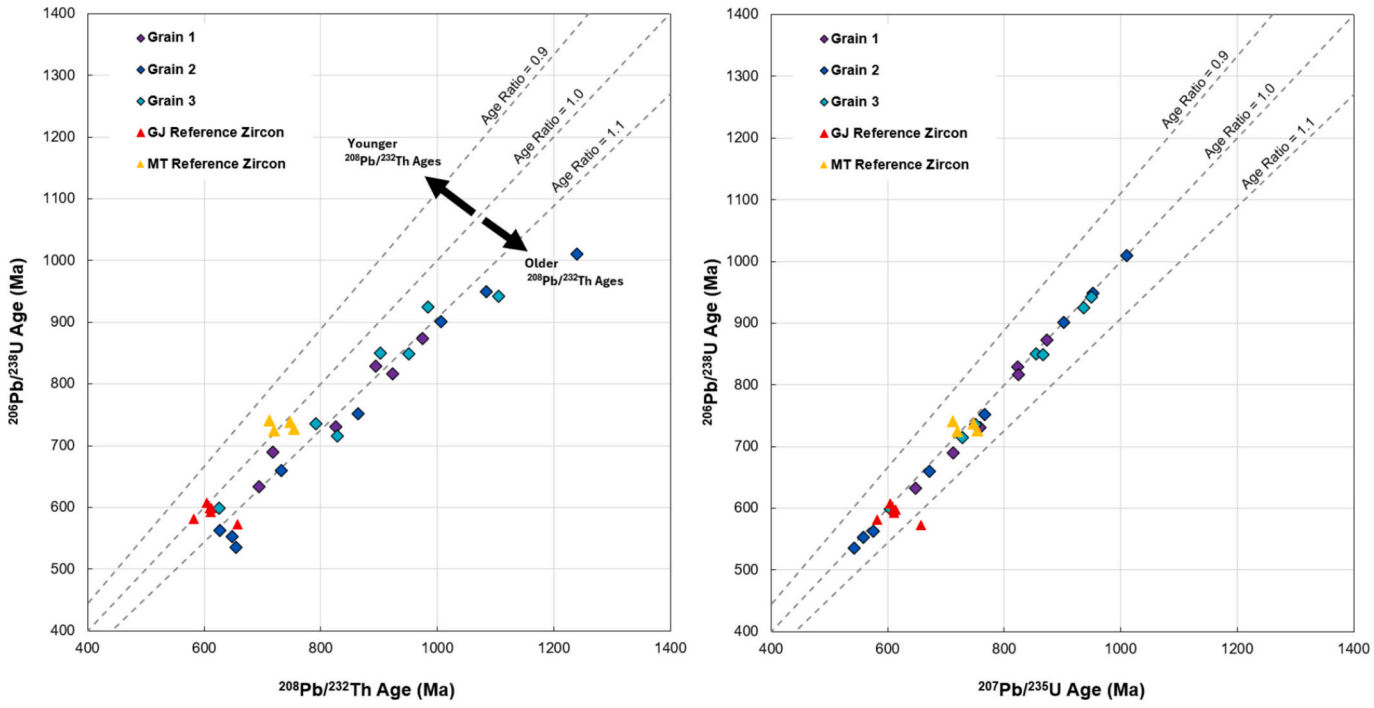

Fig. 8. Comparison of Pb—U ages and Pb—Th ages. $^{208}Pb/^{232}Th$ ages (left) are systematically shifted toward older apparent ages i.e., exhibit reverse discordance. In comparison, Pb—U ages are mostly concordant (right). For reference, GJ and MT reference zircon analyses are shown which show analyses clustering around 1.0 i.e., concordant, for both Pb—U and Pb—Th ages.

664 ppm) positively correlate with $^{206}Pb/^{238}U$ dates and Th/U values are >1.1 except for spot 1 (Th/U = 0.83) which was located on a porosity trail within blurry oscillatory zoning (Fig. 5e). The REE pattern for all seven analyses is similar, showing strong enrichment of HREE over LREE and strong Ce and Eu anomalies (Fig. 7c). Two of the analyses with the oldest measured $^{206}Pb/^{238}U$ dates (Spots 2 and 3 located within the non-porous CL-homogenous domain) have the highest total REE (771 ppm to 980 ppm), Yttrium (1215 ppm to 1557 ppm) and Titanium (15 ppm to 27 ppm) concentrations. The remaining five analyses have variable total REE (296 ppm to 532 ppm) and Yttrium (439 ppm to 799 ppm) concentrations. Titanium concentrations from spots 4 to 7 are consistently low, ranging from 5 ppm to 8 ppm. In comparison, Ti concentrations from spots 3, 2 and 1 ($^{206}Pb/^{238}U$ dates >750 Ma) are consistently higher, ranging from 14 ppm to 27 ppm. Hafnium concentrations are variable (9474 ppm to 11,468 ppm) across porous and non-porous domains and show a weakly negative correlation with $^{206}Pb/^{238}U$ dates.

In grain 3, seven analyses produced an array of concordant dates ranging from 942 ± 24 Ma to 599 ± 20 Ma (Fig. 6e, f). The oldest $^{206}Pb/^{238}U$ date of 942 ± 24 Ma came from the centre of the grain on a trail of micron-scale porosity while the youngest $^{206}Pb/^{238}U$ dates of 599 ± 20 Ma came from spot 6, which mostly covers the CL-bright rim with some overlap with the adjacent CL-dark domain (Fig. 5b). The next two youngest $^{206}Pb/^{238}U$ dates (Spot 1 and Spot 4) are located near the edge of the grain (Fig. 5b). Spots 2, 3 and 5 are located on a ~ 20 μm wide porosity trail and recorded $^{206}Pb/^{238}U$ dates of 850 ± 16 Ma, 849 ± 22 Ma, and 925 ± 14 Ma. Uranium concentrations range from 215 ppm to 779 ppm and Th/U values are variable (1.06 to 1.59) (Fig. 7b). Both U concentrations and Th/U show a weak correlation with $^{206}Pb/^{238}U$ dates. Rare earth element patterns are similar for six analyses, showing a strong enrichment of HREE over LREE and strong Ce and Eu anomalies (Fig. 7c). One analysis located on a porosity trail within the CL-dark homogenous core (Spot 3) shows a more pronounced depletion of LREE over HREE resulting in a steeper HREE profile. Total REE concentrations are variable, ranging from 511 ppm to 880 ppm and along with Ti (7 ppm to 30 ppm) and Y (567 ppm to 1425 ppm) show a positive correlation with $^{206}Pb/^{238}U$ dates. Hafnium concentrations are variable (9207 ppm to 10,945 ppm) and show a weak negative correlation with $^{206}Pb/^{238}U$ dates.

Time integrated raw (background subtracted) $^{206}Pb/^{238}U$ ratios and trace element data (Y, Ce, La, Pr, and Ti) over a 120 s ablation period for Spot 5 in grain 3 is presented in Fig. 9. Over the duration of the ablation signal, there are notable sharp peaks in Ce, La, and Pr counts (grey vertical bars, Fig. 9b). Titanium counts over this interval are also higher with peak counts corresponding with the four peaks in Ce, La and Pr (Fig. 9b).

5.4. *Theoretical determination of radiation damage*

Theoretically determined accumulated alpha doses over a period of 1000 million years for each U—Pb spot are presented in Fig. 9. Calculated alpha doses range from ~$9x10^{17}a.g^{-1}$ to $30x10^{17}a.g^{-1}$. With consideration to a period of 500 million years, calculated alpha doses range from $4.4x10^{17}a.g^{-1}$ to $15.5x10^{17}a.g^{-1}$. In both scenarios, there is no correlation between apparent U—Pb ages and calculated alpha doses (Fig. 10). Grain1 and grain 2 show three analyses each with values that are above the threshold of $22x10^{17}a.g^{-1}$ (red line, Fig. 10). This first percolation threshold as defined by Pidgeon (2014) relates to the point at which amorphous, radiation damaged domains, become interconnected, such that properties of zircon change significantly and loss of elements by diffusion and bulk dissolution occurs rapidly.

6. Discussion

6.1. *Recognition of zircon grains modified by coupled dissolution-precipitation replacement reactions*

Coupled dissolution-precipitation (CDP) is a fluid mediated mineral replacement reaction process that is driven by the need of the mineral-fluid system at the mineral-fluid interface to achieve a lower energy state (Ruiz-Agudo et al., 2014). Fluids, including melts, in contact with a mineral can induce dissolution, resulting in an interfacial boundary

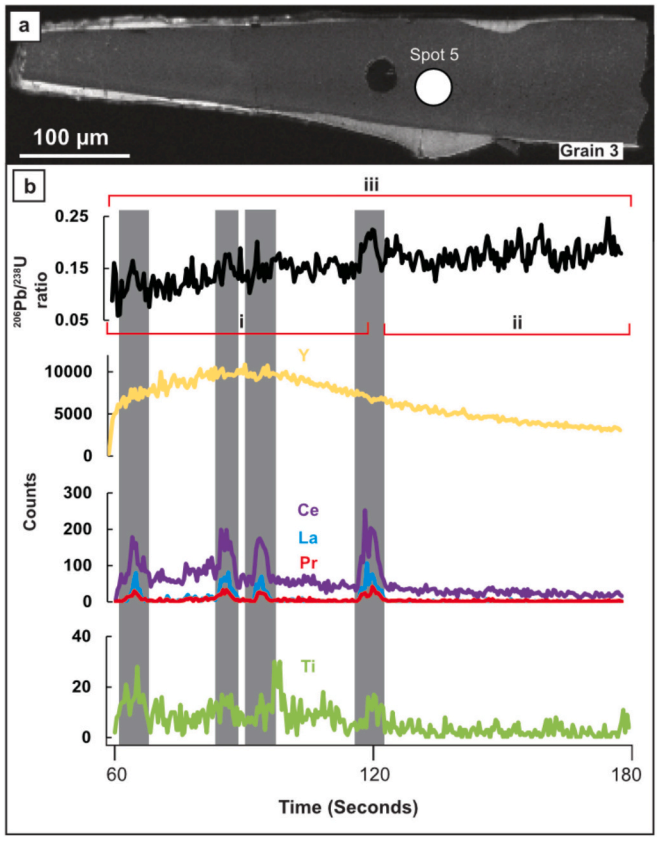

Fig. 9. Time-integrated (background subtracted) raw $^{206}Pb/^{238}U$ and trace element data (b) for Spot 5 in grain 3 (a). Grey bars highlight ablation domains based on relatively high counts in the Ce, La and Pr signals.

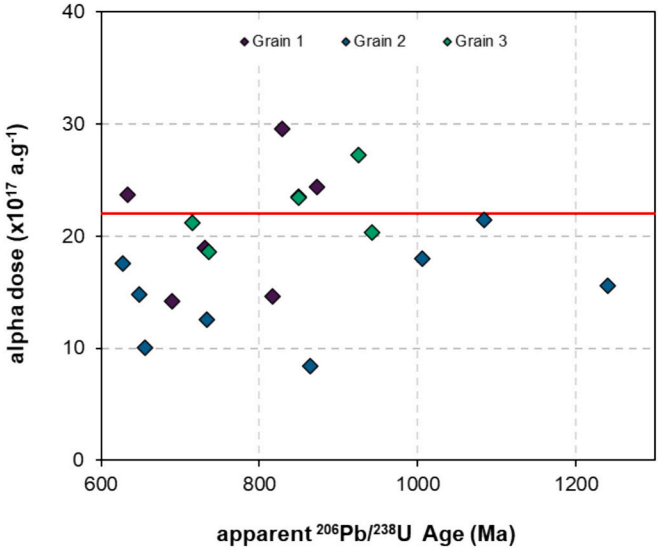

Fig. 10. Maximum theoretical alpha dose accumulated by zircon grains over 1000 Myr between crystallisation (approximated at 1050 Ma) and present day. The red line indicates the first percolation threshold of 22×10^{17} a.g^{-1} defined by Pidgeon (2014). (For interpretation of the references to colour in this figure legend, the reader is referred to the web version of this article.)

layer fluid that is supersaturated in components dissolved from the parent mineral (Putnis, 2009). A new mineral (product mineral) which is stable with respect to the fluid composition may then nucleate on the surface of the parent mineral. These reactions can involve replacement with one mineral by another, or replacement of one mineral by the same mineral which is compositionally more stable with respect to the reacting fluid. In the latter case, the likeness of the crystallographic lattice will result in an epitaxial relationship between parent and product mineral (Putnis, 2009). Inward migration of the reaction interface, eventually resulting in complete replacement of the parent mineral, can continue so long as mass transfer pathways are maintained between the sites of dissolution and the bulk fluid reservoir. In the absence of a permeable porosity network, chemical communication between the inward moving reaction interface and the bulk fluid reservoir is facilitated by multi-stage dissolution and precipitation of the product mineral which maintains a dynamic porosity network that enables continued fluid infiltration and reaction (Beaudoin et al., 2018; Norberg et al., 2011; Ruiz-Agudo et al., 2014) and stepwise approach toward an equilibrium product mineral chemistry with respect to the bulk fluid composition. Prolonged exposure to the reacting fluid promotes textural coarsening (healing of porosity) or infilling of porosity by other minerals crystallising out of the fluid phases (Spruzeniece et al., 2017b), driving the composition of the product mineral closer toward mineral-fluid equilibrium as the crystal lattice is broken apart and rebuilt over multiple cycles of dissolution and precipitation (Altree-Williams et al., 2015; Ruiz-Agudo et al., 2014).

Replacement of one mineral by the same mineral species is often referred to as 'recrystallisation'. However, we emphasise that the term recrystallisation, from a microstructural perspective, strictly refers to the rearrangement and/or appearance of grain boundaries within a crystalline material (Means, 1983) which may not necessarily involve chemical changes (Passchier and Trouw, 2005). Based on this definition, the terms 'replacement' and 'recrystallisation' are not interchangeable. True zircon recrystallisation may occur through mechanisms such as sub-grain rotation during crystal plastic deformation in shear zones (Piazolo et al., 2012), whilst chemically distinguishable core-rim structures typically form in response to dissolution-precipitation replacement processes (Rubatto et al., 2008). For clarity, we will refer to CDP modification of parent zircon and replacement by product zircon as 'zircon CDP replacement' in the following discussion.

Zircons recovered from the Macklin Island meta-gabbro show several characteristic microstructural features of fluid-mediated CDP replacement reactions (Putnis, 2009) including i) overall preservation of the precursor grain morphology with evidence of dissolution of the grains in the formation of pitted surfaces and embayed grain boundaries in cross-section (Fig. 4), ii) abundant micron-scale porosity within the interior of the grains (Fig. 5a, c, e and inset i and ii), iii) destruction or overprinting of primary growth zoning (Fig. 5f), and iv) compositionally distinct rims with sharp boundaries progressing toward the core of the grain (e.g. CL-bright rims in Fig. 5b, d and f). In addition, the studied zircons show trace element depletion associated with microstructures indicative of former CDP replacement reactions, i.e. microporosity and CL-bright rims (Fig. 5), consistent with chemical changes observed in experimental and natural examples of zircon CDP replacement (Asimus et al., 2024; Daczko et al., 2024; Martin et al., 2008; Soman et al., 2010; Tomaschek et al., 2003). In the context of zircon CDP replacement, trace element depletion arises from high structural strain in trace element enriched zircon driving enhanced dissolution of the parent zircon and precipitation of less soluble, trace element poor product zircon. Conceptually the re-equilibration of trace element rich zircon in the presence of a fluid can be understood using a simplified open-system reaction formula (Zr, Hf, Y, REE, Th, U) $(Si, P)O_4 + fluid_1 = (Zr,Hf)SiO_4 + fluid_2$, where Y, REE, Th, U and P are mobilised by and lost to the reactive fluid.

As noted by Altree-Williams et al. (2015), the microstructural expression of CDP replacement reactions is highly diverse resulting from localised boundary conditions at the reaction interface interacting with several different parameters including fluid chemistry, temperature, pressure, and reaction affinity within a dynamic chemical system. In this study, we distinguish two distinct microstructural expressions of CDP replacement reactions that have modified the parent zircon as Domain A

and Domain B with key microstructural characteristics summarised below.

Domain A shows high cathodoluminescence response (described as bleached rims by Halpin et al., 2012) with ghosted oscillatory zoning, convoluted zoning, or no zoning visible, typically forming thin, curvilinear rims truncating the interior CL-dark domain indicating reaction progressive from the outside in (Fig. 5b, d, and f). Domain A can also be observed along linear cross-cutting bands, likely representing sites of healed fractures and as discrete ovoid features in the interior of the grain that are likely connected to the rim in the third dimension (Fig. 5d, f). Porosity is rarely observed in Domain A.

Domain B shows low cathodoluminescence response, typically unzoned, though some blurred oscillatory zoning can be preserved (Fig. 5d, with micro-porosity transgressing the interior of the grains. Except for Spot 6 in Grain 3, all spot data from grains 1, 2, 3 are considered part of Domain B. Areas of blurred oscillatory zoning are truncated by homogenous, unzoned CL-dark zircon on one side and by Domain A rim zircon on the other side (Fig. 5, inset iii). This microstructural pattern implies progression of multiple reaction fronts in different directions at different times. Domain A reaction front produces a 'core-rim' texture whereas internal to Domain B, there are additional reaction fronts preserved (Fig. 5, inset iii). Multiple and cross-cutting reaction fronts are the product of a chemically dynamic system during which the zircon lattice is broken down and rebuilt during multiple stages of CDP, progressing toward an 'equilibrium composition'.

In the Halpin et al. (2012) study, it was recognised that the bleached rims (Domain A in this study) represented modification of zircon, but the cores were thought to be unmodified due to lack of distinguishing microstructures observed in the overview CL and BSE images, typically taken at the grain to multi-grain scale. In this study we investigated the microstructure within Domain B in detail as this is the domain that was probed by U—Pb dating that showed the array of U—Pb dates. Our data from Domain B indicates that the entire domain has been replaced by zircon CDP replacement processes and there is likely no preservation of unmodified parent zircon. This interpretation is consistent with the trace element depletion observed in both domains A and B (Fig. 7). Additionally, multiple spot analyses within a single grain show heterogeneity of chemistry and age (Fig. 5–7).

6.2. Assessing the potential for enhanced Pb mobility through diffusion-controlled mechanisms

In this section we assess and discuss the potential for enhanced Pb mobility through diffusion-controlled mechanisms as an alternative model to explain the observed isotope and trace element patterns.

Radioactive alpha-decay events in the U and Th series generate both highly energetic alpha-particles and less-energetic but more destructive recoil nuclei. Given enough time and with high enough concentration of U and Th, zircon can accumulate significant radiation damage which can disrupt the lattice enough to greatly enhance Pb mobility. Progressive radiation damage may reach an important stage, defined as the first percolation point (Salje et al., 1999), whereby radiation damaged (amorphous) domains in the zircon forms an interconnected percolating network within the crystal lattice. Salje et al. (1999) defined this threshold based on an alpha decay dose of 35×10^{17} a.g^{-1} (alpha-decay events per gram), which was subsequently revised to 22×10^{17} a.g^{-1} (Pidgeon, 2014). Calculated alpha doses accumulated for 500 million years (4.4×10^{17} a.g^{-1} to 15.6×10^{17} a.g^{-1}) fall well below the threshold for significant radiation damage of 22×10^{17} a.g^{-1}. For a duration of 1000 million years, only five of the twenty-one analyses had alpha doses greater than the first percolation threshold but showed no correlation with apparent $^{206}Pb/^{238}U$ ages (Fig. 10). This is consistent with the local metamictisation at the scale of 25–30 μm observed by Halpin et al. (2012, Suppl. Material 5f). Importantly, within a single grain only a low number of analyses are above the threshold. In other words, even with localised areas of metamictisation, these damaged areas show no connectivity to the environment surrounding the zircon, i.e. allow only for very local Pb movement within the scale of an analysis spot. On this basis, Pb mobility at a scale above 30 μm is not attributable to the accumulation of radiation damage.

Additionally, diffusion-controlled Pb loss through radiation damage would predict systematically younger Th—Pb ages over U—Pb ages due to the higher kinetic energy of alpha particles and recoil nuclei from the ^{232}Th decay chain. In contrast, our results show Th—Pb ages are reversely discordant and consistently older than corresponding U—Pb ages, Fig. 8. This pattern is incompatible with a diffusion-controlled mechanisms and instead points toward fluid interaction to explain the apparent gain of Th.

6.3. Element mobility resulting from zircon CDP replacement forms complex U—Pb age arrays and trace elemental variability

In each studied grain, multiple U—Pb analyses within Domain B produced a continuum of $^{206}Pb/^{238}U$ dates spanning hundreds of millions of years (Fig. 5 and Fig. 6), replicating the spread of U—Pb dates reported by Halpin et al. (2012) based on a population of 56 grains. Domain B shows significant variation in both U—Pb dates and trace element concentrations. As $^{206}Pb/^{238}U$ dates become younger, there is a clear trend of decreasing REE, Y, Th, U, and Ti (Fig. 7) indicating active trace element and Pb movement during melt-mediated CDP replacement. The 50 μm spot analysis averages the composition of the ablated volumes, but spikes in trace element signals (Fig. 9) suggest the presence of micro-inclusions or localised enrichment within microdomains. Overall, the bulk volume of ablated zircon which produced younger U—Pb dates is relatively poor in trace elements.

In contrast to trace elements (REE, Y, U, Th and Pb), Hf isomorphically substitutes Zr in the crystalline lattice and is assumed to be compatible within the product zircon. Hafnium concentrations measured in this study show either a slight increase in the concentration with progressive younger apparent U—Pb ages, or no significant change indicating that existing Hf will be retained in the product zircon and if available, exogenous Hf in the reactive melt can be incorporated into the product zircon. As demonstrated in the Halpin et al. (2012) study, zircons from the meta-gabbro exhibit a narrow range of $^{176}Hf/^{177}Hf_i$ values with no correlation with Pb-loss (one spot analysis per grain). Such a relationship may suggest that the Hf isotopic system was largely unperturbed during the process of melt-mediated CDP. However, we note that the intra-grain Hf isotopic variability was not measured in this study and therefore a conclusive view on this cannot be determined. Given the apparent trend of increasing Hf concentration with progressive Pb-loss, the process of melt-mediated CDP could be expected to change the Hf isotopic signature of the precursor depending on the amount of exogenous Hf incorporated into the crystal lattice of the product zircon and the difference between the Hf isotopic composition of the precursor zircon and reactive melt. Similarly, the observed shift to older Pb/Th dates shown in Fig. 9 may indicate Th exchange with the reactive melt during CDP or alternatively, ablation of Th-rich micro inclusions formed via intra-grain redistribution of Th during CDP.

With consideration to zircon CDP replacement, the observed heterogenous chemistry in both isotopes and trace elements in our study can result from a combination of (1) ablation of mixtures of parent and product zircon (Grand'Homme et al., 2016), (2) modification involving an evolving fluid (closed-system) or different fluid compositions (open-system) with contrasting capacities to mobilise trace elements and Pb, (3) variable maturity of the product mineral linked to different exposure to the bulk fluid in terms of time and chemical communication (Borg et al., 2014; Spruzeniece et al., 2017a; Varga et al., 2020) and (4) mixture of the latter variably mature reaction products as porosity is transient during CDP and may be infilled by a different chemistry during the evolution of CDP (e.g. Spruzeniece et al., 2017a). The variability of the chemical signal with duration of analysis points to chemical variations at a spatial resolution of less than 2 μm which is in the order of

magnitude of the porosity seen (Fig. 5, inset i), ii)). Furthermore, chemical heterogeneity could also develop after the CDP process as the porosity may enhance later diffusion of trace elements and Pb or localise deformation microstructures or fractures that acts as fast diffusion pathways (e.g. Reddy et al., 2006; Piazolo et al., 2012; Timms et al., 2006; Daczko et al., 2024).

Fig. 11 presents a schematic model showing the development of the observed reaction textures and chemical patterns during melt-mediated CDP replacement. Redistribution of Pb within the product zircon and Pb-loss from the grain to the bulk fluid results in incomplete U—Pb isotopic resetting. When the trace element enriched parent zircon dissolves, elements that are more soluble, and less compatible in the product zircon (Ti, Y, REE, P, U, Th and Pb) will favourably partition into the fluid phase where they are transported through the network of fluid-filled porosity from the reaction front to the bulk fluid. However, these incompatible elements may be temporarily sequestered into transient micro-inclusions. How efficiently these elements exchange with the bulk fluid is therefore dependent on the following factors: (i) compatibility of elements in the precipitating product zircon; (ii) solubility of elements into the local boundary fluid; (iii) diffusivity of these elements through the fluid filled porosity network as determined by the chemical gradient between the reaction interface and bulk fluid reservoir; (iv) connectivity of the fluid network, and (iv) precipitation of micro-inclusions within the product zircon and their stability during multi-stage CDP.

The complex inter-relationships between the above factors results in a near continuous smear of spot dates that spread from the age of the parent zircon to the age of the CDP event though the lack of preservation of unmodified parent zircon inhibits determination of the original age. However, the oldest analysis of ca. 1050 Ma could be interpreted as a minimum estimate (Halpin et al., 2012) while the youngest date in the array of ca. 535 Ma may date the timing of CDP. Additionally, if CDP microstructures, including porosity, make the zircon susceptible to ongoing Pb-loss, the youngest date may reflect Pb mobility during subsequent thermal or fluid interaction events. However, the fact that younger ages are concordant demonstrates that Pb does not continuously "leak" from zircon replaced by CDP in the absence of subsequent geological events.

6.4. *Reaction history of the Macklin Island meta-gabbro and timing of zircon CDP*

Linking the CDP replacement microstructures in zircon to the

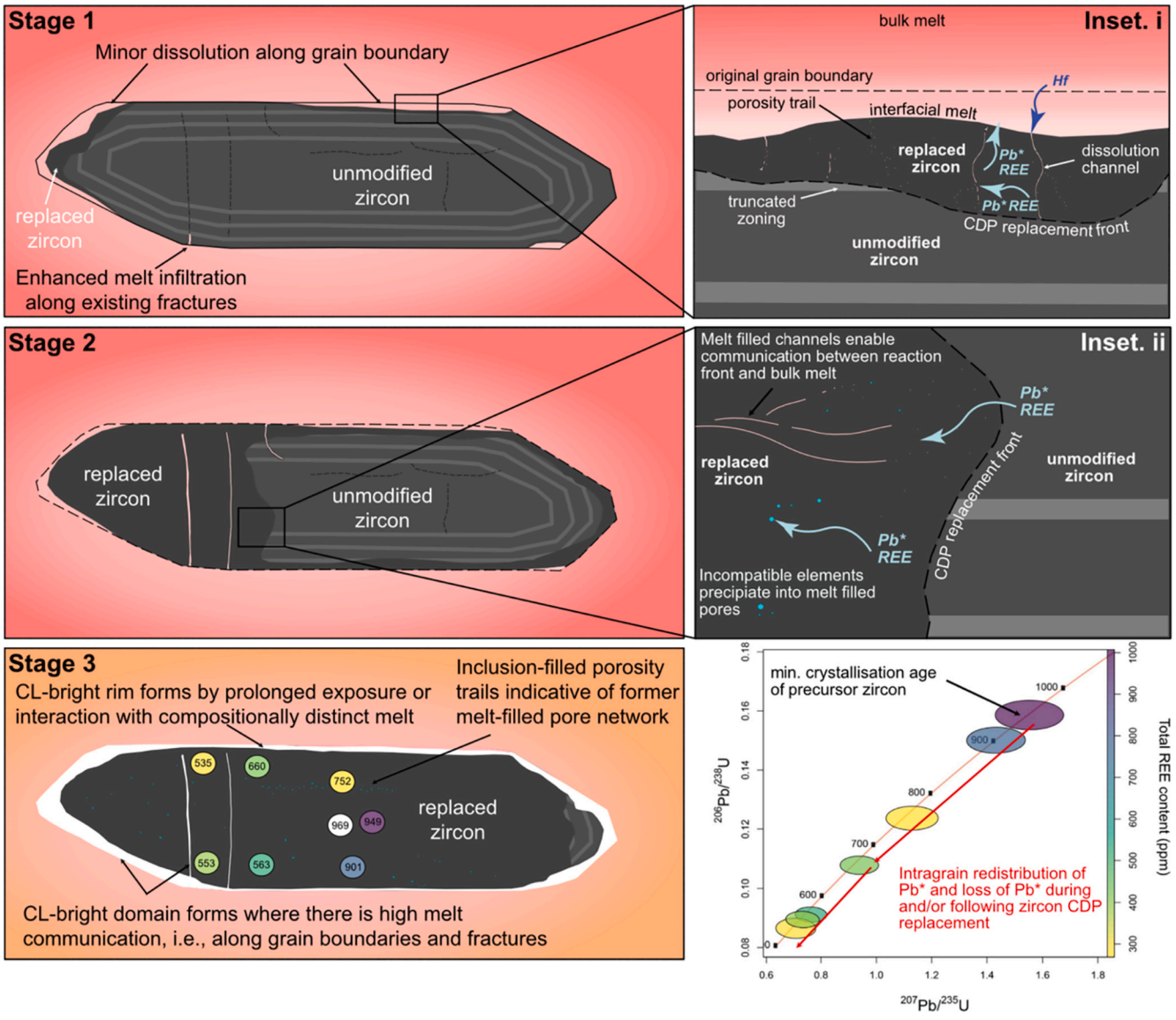

Fig. 11. Cartoon showing the development of zircon coupled dissolution-precipitation replacement of a typical grain from the Macklin Island meta-gabbro.

metamorphic and reaction history of the host rock is critical for developing a robust interpretation of the geological significance of U—Pb dates. In this section, we place zircon CDP replacement microstructures within the context of silicate reaction textures observed in the Macklin Island meta-gabbro and within the broader regional geological context.

Reaction textures in LM12 are both fine-grained and coarse-grained, discontinuous, and typically hydrous with pyroxene grains been replaced by biotite or fine-grained aggregates of quartz-feldspar-biotite (Fig. 3b, c and d). Microstructures indicative of the former presence of melt including low-dihedral angles, quartz or plagioclase films (Fig. 3b), and orthopyroxene forming 'string of beads' textures along grain boundaries (Fig. 3 inset iii), and embayments into existing minerals (Fig. 3b and Fig. 3 inset i) in the reaction textures indicate melt as the likely reactive agent (Stuart et al., 2016). High-grade melt-rock interaction is further supported by stability of pyroxene in the reaction products. Undulose extinction in both plagioclase and pyroxene, deformation twinning in plagioclase, and sutured grain boundaries between adjacent plagioclase grains with or without fine-grained neoblasts (Fig. 3a) are consistent with the existing interpretation of *syn*-tectonic, dynamic recrystallisation of charnockites during the Rayner Orogeny. However, a clear relationship between the timing of melt-rock reaction microstructures relative to solid-state deformation is difficult to establish.

With consideration to the established geological history of the Mawson Coast, we highlight three plausible scenarios where melt-rock interaction could have formed the observed CDP reaction textures, replacing xenocrystic or primary zircon:

1. Interaction with a late stage, fractionated and hydrous melt related to emplacement of the Mawson Charnockite plutonic complex where pyroxenes are preserved, and biotite is introduced.
2. Interaction with fluxing high-temperature melts related to high-grade metamorphism, crustal melting, and extensive magmatism during the 1200 Ma - 900 Ma Rayner Orogeny.
3. Interaction with fluxing high-temperature charnockite melts related to the 650 Ma - 500 Ma Kuunga Orogeny (Mikhalsky and Kamenev, 2013), where orthopyroxene is stable.

Given that there are three plausible scenarios in which melt-rock interaction could have occurred, the timing of zircon-melt interaction is ambiguous. This is partly due to the disconnect between the degree of zircon modification and rock modification where the rock reaction textures are volumetrically small compared to the extensive modification of zircon grains. Such a relationship would suggest that the host magma drove the CDP modification e.g., modification of xenocrystic zircon cargo in the Bruce Rise granite (Halpin et al., 2020). In this interpretation (scenario 1 above), all zircons in LM12 are either foreign crystals entrained in the host magma or zircons that have crystallised from preceding pulses of magma resulting in the formation of Domain A and B reaction textures, Stages 1–3 in Fig. 11. Redistribution of radiogenic Pb within a grain during CDP results in either a negligible or minor shift in ages toward the emplacement age of the host plutonic rock. However, the process of zircon CDP replacement makes the zircon grains more susceptible to Pb-loss during subsequent geological events under high temperature or fluid present conditions due to the presence of interconnected micro- to nano-scale porosity distributed throughout the grain in a process akin to deformation induced pipe diffusion (Piazolo et al., 2012). The resultant age array may therefore reflect enhanced Pb-diffusion and Pb-loss during both the 650 Ma – 500 Ma Kuunga Orogeny and during the 1200 Ma – 900 Ma Rayner Orogeny.

In scenario 2, melt-rock interaction occurring at the later stage of the Rayner Orogeny (closer to 900 Ma), could have formed the observed reaction textures. The age array in this scenario would reflect Pb-loss during melt-mediated CDP modification of primary zircons down to ~900 Ma, followed by enhanced Pb-diffusion and Pb-loss during the 650 Ma – 500 Ma Kuunga Orogeny. Alternatively, in scenario 3, Domain A and B, stages 1–3 in Fig. 11, could be interpreted to have formed during the interaction with younger melts migrating through the Mawson Charnockite during 650 Ma – 500 Ma Kuunga Orogeny. In this scenario, the age array reflects variable Pb-loss during a single episode of zircon-melt interaction, followed by more recent Pb-loss that utilises a porosity network that formed about a half a billion years earlier.

Reconciling zircon CDP reaction textures with the broader metamorphic and reaction history of the Macklin Island meta-gabbro requires in-situ textural characterisation of zircon in relation to melt-rock reaction textures. As there is a lack of clear evidence for a younger, Kuunga aged melt-reaction texture overprinting the meta-gabbro, where zircon CDP is only observed in proximity to the reaction texture, e.g. garnet-reaction zone around cross-cutting dykes in the Pembroke gabbroic gneiss (Daczko et al., 2024), we argue in favour of melt-mediated CDP occurring during formation, ascent, and emplacement of the gabbro which made the grains more susceptible to Pb mobility in subsequent metamorphic events including the Rayner Orogeny and Kuunga Orogeny.

6.5. *Implications for understanding the geochronological framework in East Antarctica*

Based on our interpretation that the apparent "smearing" of concordant zircon age arrays reflects melt-mediated CDP reactions in LM12, rather than protracted magmatism or metamorphism, it is reasonable to infer that previously obtained U—Pb zircon ages from across the Rayner Complex may be similarly affected. Supplementary Table 3 presents an extensive, though not exhaustive, compilation of published U—Pb zircon ages that have contributed significantly to the development of the Rayner Complex geological framework. This regional synthesis shows that a substantial proportion of published datasets display analytical characteristics consistent with zircon systems modified by CDP processes. In particular, the widespread occurrence of near-concordant age arrays spanning ~100 Myr (ca. 1000–900 Ma) in high-temperature orthogneisses, paragneisses, and charnockites raises the possibility that many of these datasets do not simply record zircon growth during prolonged metamorphism and magmatism.

However, many existing studies lack detailed microstructural and textural characterisation of zircon, and where such information is provided, BSE and CL images are commonly of insufficient resolution to resolve fine-scale porosity. Consequently, it is not possible to confidently attribute most existing age arrays to melt-mediated CDP processes. In this context, the Macklin Island metagabbro is distinctive, both in the extent of its U—Pb age dispersion and in the clear linkage between zircon microstructure and complex U—Pb isotope and trace-element systematics. Unlike many regional studies that rely on single-spot analyses per grain, this dataset documents systematic intra-grain age arrays that can be directly linked to specific CDP-related microstructures, including microporosity, truncated zoning, and complex reaction fronts revealed by high-resolution BSE and CL imaging of individual zircon grains.

Given the ubiquity of high-temperature melting, melt migration, and melt–rock interaction during the Rayner Orogeny, and the potential for further modification during the Kuunga Orogeny, it is likely that CDP processes have affected zircon U—Pb systematics to varying degrees across the province. Accordingly, many previously published U—Pb ages, particularly those defined by age arrays rather than discrete concordant populations, or those forming discordia with well-defined upper and lower intercepts, may reflect zircon modification by CDP replacement. This does not invalidate the existing geochronological framework for the Rayner Complex. However, it does imply that individual zircon U—Pb datasets may be more complex than previously assumed. In particular, ages reported between the two orogenic events (ca. 900–600 Ma) should be treated with caution, as they may not record discrete geological events but instead reflect partial isotopic resetting or mixing associated with CDP processes. Collectively, these observations

highlight the need for future geochronological studies in the Rayner Complex, and in comparable high-grade metamorphic terranes, to explicitly assess the potential role of CDP replacement and to account for the additional complexity it introduces into age interpretations. This requires careful evaluation of zircon microstructures and systematic integration of trace-element systematics with U—Pb geochronology.

7. Conclusion

Zircons recovered from the Macklin Island meta-gabbro have been extensively replaced through the process of melt-mediated CDP resulting in spurious U—Pb spot ages forming a near-concordant age array spanning hundreds of millions of years. In previous studies, CDP processes were attributed to the formation of CL-bright rims. However, the extensive nature of CDP modification of zircons from the meta-gabbro was not recognised, and therefore, the underlying mechanism causing complex age patterns were erroneously interpreted. Given the considerable impact of CDP on zircon U—Pb geochronology, recognising evidence of CDP replacement reactions is critical for interpreting the geological significance of complex age patterns such as near-concordant age arrays typical of high-temperature metamorphic terranes where melting and melt-migration occur.

Geochemically important trace elements including the rare earth elements, thorium and titanium are also variably redistributed and depleted during CDP. Consequently, trace element spot analyses in zircon grains modified by CDP can yield spurious geochemical information which need to be carefully considered when applying geochemical tools such as Ti-in-zircon thermometry to derive geologically meaningful information.

Based on our study of the Macklin Island meta-gabbro, we highlight key microstructures and chemical patterns that can be used to recognise melt-mediated CDP in zircon including:

- Microstructures
  - o Modified CL textures e.g. blurred CL to homogenous CL as well as truncated and cross-cutting features,
  - o Porosity forming trails, and clustered or dispersed patterns,
  - o Dissolution features at grain boundaries e.g., curvilinear, embayed grain boundaries and pitting,
  - o Micro inclusions, either directly observed or inferred from chemistry.
- Chemical patterns
  - o Intra-grain chemical and isotopic heterogeneity within a defined textural domain,
  - o General depletion of trace elements and Pb,
  - o More complex behaviour for Hf with little to no change in the reaction product compared to parent grain,
  - o Decoupling of U—Pb and Hf—Lu isotopic systems.

The simplest interpretation of ages from domains of zircon CDP replacement is that the oldest concordant ages date the crystallisation age of the precursor grain and the youngest concordant ages date the CDP event. Complications in age interpretation arise if zircons are all inherited xenocrysts or antecrysts and where there are multiple high-temperature metamorphic events, as is the case for the Macklin Island meta-gabbro, where the near concordant age array can be interpreted as the result of melt-mediated CDP modification occurring during emplacement of the parental magma or through interaction of migrating melts during subsequent geological events including the Rayner Orogeny and the Kuunga Orogeny. In such cases, understanding the timing of CDP would require zircon CDP textures to be linked to the broader reaction history of the rock.

CRediT authorship contribution statement

Jean-Antoine Gazi: Writing – original draft, Visualization, Formal analysis, Conceptualization. **Nathan R. Daczko:** Writing – review & editing, Supervision, Formal analysis, Conceptualization. **Elena Belousova:** Resources, Methodology, Investigation. **Jacqueline A. Halpin:** Writing – review & editing, Resources. **Sandra Piazolo:** Writing – review & editing, Conceptualization.

Declaration of competing interest

The authors declare the following financial interests/personal relationships which may be considered as potential competing interests:

Jacqueline Halpin reports financial support was provided by Australian Centre for Excellence in Antarctic Science. If there are other authors, they declare that they have no known competing financial interests or personal relationships that could have appeared to influence the work reported in this paper.

Acknowledgements

This work builds on data collected by Aaron Flint as part of a small research unit of study at Macquarie University supervised by Elena Belousova. We acknowledge Steven Craven, Manal Bebbington, Will Powell, David Adams, Rosanna Murphy, Sarah Gain, Nicole McGowan, Sean Murray, Yi-Jen Lai and Yoann Greau for facilitating laboratory analyses. We thank Luke Milan for providing constructive discussion about the Mawson Charnockite. This study was financially supported by the Australian Research Council Special Research Initiative, Australian Centre for Excellence in Antarctic Science (Project Number SR200100008) and internally through the School of Natural Sciences, Macquarie University. We thank the reviewers for their careful and constructive reviews and the editor for editorial handling.

Appendix A. Supplementary data

Supplementary data to this article can be found online at https://doi.org/10.1016/j.chemgeo.2026.123383.

Data availability

Data will be made available on request.

References

Altree-Williams, A., Pring, A., Ngothai, Y., Brugger, J., 2015. Textural and compositional complexities resulting from coupled dissolution–reprecipitation reactions in geomaterials. Earth Sci. Rev. 150, 628–651.

Asimus, Jeremy L., et al., 2024. Experimental replacement of Zircon by melt-mediated coupled dissolution-precipitation causes dispersion in U–Pb ages. J. Metamorph. Geol. 42 (9), 1179–1195.

Australia. Bureau of Mineral Resources, G., Geophysics, 1967. In: Trail, D.S., Swoboda, R. A., Australia. Division of National, M (Eds.), Mawson and Mount Henderson [Cartographic Material] / Base Map Compiled by the Antarctic Mapping Branch, Department of National Development ; Geology, 1954–1965 by P.W. Crohn … [et al.]; Compiled 1967 by D.S. Trail; Cartography and Drawn, 1967, by R. Swoboda. Compiled and issued by the Bureau of Mineral Resources, Geology and Geophysics, Dept. of National Development, Canberra.

Beaudoin, N., Hamilton, A., Koehn, D., Shipton, Z.K., Kelka, U., 2018. Reaction-induced porosity fingering: replacement dynamic and porosity evolution in the KBr-KCl system. Geochim. Cosmochim. Acta 232, 163–180.

Belousova, E., Griffin, W.L., O'Reilly, S.Y., Fisher, N., 2002. Igneous zircon: trace element composition as an indicator of source rock type. Contrib. Mineral. Petrol. 143 (5), 602–622.

Belousova, E., et al., 2010. The growth of the continental crust: constraints from zircon Hf-isotope data. Lithos 119 (3–4), 457–466.

Boger, S.D., 2011. Antarctica—before and after Gondwana. Gondwana Res. 19 (2), 335–371.

Boger, S.D., et al., 2002. Pan-African intraplate deformation in the northern Prince Charles Mountains, East Antarctica. Earth Planet. Sci. Lett. 195 (3–4), 195–210.

Borg, S., Liu, W., Pearce, M., Cleverley, J., MacRae, C., 2014. Complex mineral zoning patterns caused by ultra-local equilibrium at reaction interfaces. Geology 42 (5), 415–418.

Cherniak, D., Watson, E., 2001. Pb diffusion in zircon. Chem. Geol. 172 (1–2), 5–24.

Cherniak, D.J., Watson, E.B., 2003. Diffusion in zircon. Rev. Mineral. Geochem. 53 (1), 113–143.

Cherniak, D., Watson, E., 2007. Ti diffusion in zircon. Chem. Geol. 242 (3–4), 470–483.
Clark, C., Taylor, R.J., Kylander-Clark, A.R., Hacker, B.R., 2018. Prolonged (> 100 Ma) ultrahigh temperature metamorphism in the Napier Complex, East Antarctica: a petrochronological investigation of Earth's hottest crust. J. Metamorph. Geol. 36 (9), 1117–1139.
Condit, C.B., Mahan, K.H., Curtis, K.C., Möller, A., 2018. Dating metasomatism: monazite and zircon growth during amphibolite facies albitization. Minerals 8 (5), 187.
Crohn, P., 1959. A Contribution to the Geology and Glaciology of the Western Part of Australian Antarctic Territory. Antarctic Division, Department of External Affairs.
Daczko, N.R., Halpin, J.A., 2025. Gondwanan continental collision drives gravitational spreading and collapse of the ancestral East Antarctic mountains. Earth Planet. Sci. Lett. 662, 119394.
Daczko, N.R., Halpin, J.A., Fitzsimons, I.C., Whittaker, J.M., 2018. A cryptic Gondwana-forming orogen located in Antarctica. Sci. Rep. 8 (1), 1–9.
Daczko, Nathan R., Elliott, V., Piazolo, S., Hao, K., 2024. Zircon coupled dissolution–precipitation replacement during melt–rock interaction modifies chemical signatures resulting in misleading ages. J. Metamorph. Geol. 42 (9), 1197–1214.
Dunkley, D., Clarke, G., White, R., 2002. Structural and metamorphic evolution of the mid-late Proterozoic Rayner Complex, Cape Bruce, east Antarctica, Antarctica at the close of a millennium. In: Proceedings of the 8th International Symposium on Antarctic Earth Sciences, Wellington 1999.
Ferry, J.M., Watson, E.B., 2007. New thermodynamic models and revised calibrations for the Ti-in-zircon and Zr-in-rutile thermometers. Contrib. Mineral. Petrol. 154 (4), 429–437.
Fitzsimons, I., 2000. Grenville-age basement provinces in East Antarctica: evidence for three separate collisional orogens. Geology 28 (10), 879–882.
Geisler, T., Schaltegger, U., Tomaschek, F., 2007. Re-equilibration of zircon in aqueous fluids and melts. Elements 3 (1), 43–50.
Ginster, U., Reiners, P.W., Nasdala, L., Chanmuang, C., 2019. Annealing kinetics of radiation damage in zircon. Geochim. Cosmochim. Acta 249, 225–246.
Grand'Homme, A., et al., 2016. Partial resetting of the U-Th-Pb systems in experimentally altered monazite: nanoscale evidence of incomplete replacement. Geology 44 (6), 431–434.
Griffin, W., 2008. GLITTER: data reduction software for laser ablation ICP-MS. In: Laser Ablation ICP-MS in the Earth Sciences: Current Practices and Outstanding Issues, pp. 308–311.
Halpin, J., Gerakiteys, C., Clarke, G., Belousova, E., Griffin, W., 2005. In-situ U–Pb geochronology and Hf isotope analyses of the Rayner Complex, east Antarctica. Contrib. Mineral. Petrol. 148 (6), 689–706.
Halpin, J.A., Clarke, G., White, R., Kelsey, D., 2007. Contrasting p–t–t paths for Neoproterozoic metamorphism in MacRobertson and Kemp Lands, east Antarctica. J. Metamorph. Geol. 25 (6), 683–701.
Halpin, J., Daczko, N., Milan, L., Clarke, G., 2012. Decoding near-concordant U–Pb zircon ages spanning several hundred million years: recrystallisation, metamictisation or diffusion? Contrib. Mineral. Petrol. 163 (1), 67–85.
Halpin, J., et al., 2020. Provenance of rifted continental crust at the nexus of East Gondwana breakup. Lithos 354, 105363.
Hoskin, P.W., Schaltegger, U., 2003. The composition of zircon and igneous and metamorphic petrogenesis. Rev. Mineral. Geochem. 53 (1), 27–62.
Jackson, S.E., Pearson, N.J., Griffin, W.L., Belousova, E.A., 2004. The application of laser ablation-inductively coupled plasma-mass spectrometry to in situ U–Pb zircon geochronology. Chem. Geol. 211 (1–2), 47–69.
Kelly, N., Clarke, G., Fanning, C., 2004. Archaean crust in the Rayner Complex of east Antarctica: Oygarden group of islands, Kemp Land. Earth Environ. Sci. Trans. R. Soc. Edinb. 95 (3–4), 491–510.
Korhonen, F., Clark, C., Brown, M., Bhattacharya, S., Taylor, R., 2013. How long-lived is ultrahigh temperature (UHT) metamorphism? Constraints from zircon and monazite geochronology in the Eastern Ghats orogenic belt, India. Precambrian Res. 234, 322–350.
Kramers, J., Frei, R., Newville, M., Kober, B., Villa, I., 2009. On the valency state of radiogenic lead in zircon and its consequences. Chem. Geol. 261 (1–2), 4–11.
Laurent, A.T., et al., 2018. Decoding a protracted zircon geochronological record in ultrahigh temperature granulite, and persistence of partial melting in the crust, Rogaland, Norway. Contrib. Mineral. Petrol. 173 (4).
Li, Z.-X., et al., 2008. Assembly, configuration, and break-up history of Rodinia: a synthesis. Precambrian Res. 160 (1–2), 179–210.
Liu, X., et al., 2006. Late Pan-African granitoids from the Grove Mountains, East Antarctica: age, origin and tectonic implications. Precambrian Res. 145 (1–2), 131–154.
Liudong, R., Shi, Z., Yanbin, W., Chong, L., 2018. Distribution domains of the Pan-African event in East Antarctica and adjacent areas. Adv. Polar Sci. 87–107.
Martin, L.A., Duchêne, S., Deloule, E., Vanderhaeghe, O., 2008. Mobility of trace elements and oxygen in zircon during metamorphism: consequences for geochemical tracing. Earth Planet. Sci. Lett. 267 (1–2), 161–174.
Means, W., 1983. Microstructure and micromotion in recrystallization flow of octachloropropane: a first look. Geol. Rundsch. 72, 511–528.
Meek, U., Piazolo, S., Daczko, N.R., 2019. The field and microstructural signatures of deformation-assisted melt transfer: insights from magmatic arc lower crust, New Zealand. J. Metamorph. Geol. 37 (6), 795–821.
Merdith, A.S., et al., 2017. A full-plate global reconstruction of the Neoproterozoic. Gondwana Res. 50, 84–134.
Mezger, K., Krogstad, E., 1997. Interpretation of discordant U-Pb zircon ages: an evaluation. J. Metamorph. Geol. 15 (1), 127–140.
Mikhalsky, E., Kamenev, I., 2013. Recurrent transitional group charnockites in the east Amery Ice Shelf coast (East Antarctica): petrogenesis and implications on tectonic evolution. Lithos 175, 230–243.
Miller, J.S., Matzel, J.E., Miller, C.F., Burgess, S.D., Miller, R.B., 2007. Zircon growth and recycling during the assembly of large, composite arc plutons. J. Volcanol. Geotherm. Res. 167 (1–4), 282–299.
Möller, A., O'Brien, P.J., Kennedy, A., Kröner, A., 2002. Polyphase zircon in ultrahigh-temperature granulites (Rogaland, SW Norway): constraints for Pb diffusion in zircon. J. Metamorph. Geol. 20 (8), 727–740.
Möller, A., O'Brien, P.J., Kennedy, A., Kröner, A., 2003. Linking growth episodes of zircon and metamorphic textures to zircon chemistry: an example from the ultrahigh-temperature granulites of Rogaland (SW Norway). Geol. Soc. Lond. Spec. Publ. 220 (1), 65–81.
Mulder, J.A., et al., 2019. A Multiproxy provenance approach to uncovering the assembly of East Gondwana in Antarctica. Geology 47 (7), 645–649.
Nasdala, L., Wenzel, M., Vavra, G., Irmer, G., Wenzel, T., Kober, B., 2001. Metamictisation of natural zircon: accumulation versus thermal annealing of radioactivity-induced damage. Contrib. Mineral. Petrol. 141 (2), 125–144.
Norberg, N., Neusser, G., Wirth, R., Harlov, D., 2011. Microstructural evolution during experimental albitization of K-rich alkali feldspar. Contrib. Mineral. Petrol. 162 (3), 531–546.
Passchier, C.W., Trouw, R.A., 2005. Microtectonics. Springer Science & Business Media.
Paterson, B.A., et al., 1992. The nature of zircon inheritance in two granite plutons. Earth Environ. Sci. Trans. R. Soc. Edinb. 83 (1–2), 459–471.
Piazolo, S., Austrheim, H., Whitehouse, M., 2012. Brittle-ductile microfabrics in naturally deformed zircon: deformation mechanisms and consequences for U-Pb dating. Am. Mineral. 97 (10), 1544–1563.
Phillips, G., Kelsey, D.E., Corvino, A.F., Dutch, R.A., 2009. Continental reworking during overprinting orogenic events, southern Prince Charles Mountains, East Antarctica. J. Petrol. 50 (11), 2017–2041.
Piazolo, S., et al., 2016. Deformation-induced trace element redistribution in zircon revealed using atom probe tomography. Nat. Commun. 7 (1), 1–7.
Pidgeon, R., 2014. Zircon radiation damage ages. Chem. Geol. 367, 13–22.
Putnis, A., 2009. Mineral replacement reactions. Rev. Mineral. Geochem. 70 (1), 87–124.
Reddy, S.M., et al., 2006. Crystal-plastic deformation of zircon: a defect in the assumption of chemical robustness. Geology 34 (4), 257–260.
Rubatto, D., Hermann, J., 2003. Zircon formation during fluid circulation in eclogites (Monviso, Western Alps): implications for Zr and Hf budget in subduction zones. Geochim. Cosmochim. Acta 67 (12), 2173–2187.
Rubatto, D., Müntener, O., Barnhoorn, A., Gregory, C., 2008. Dissolution-reprecipitation of zircon at low-temperature, high-pressure conditions (Lanzo Massif, Italy). Am. Mineral. 93 (10), 1519–1529.
Ruiz-Agudo, E., Putnis, C., Putnis, A., 2014. Coupled dissolution and precipitation at mineral–fluid interfaces. Chem. Geol. 383, 132–146.
Salje, E., Chrosch, J., Ewing, R., 1999. Is "metamictization" of zircon a phase transition? Am. Mineral. 84 (7–8), 1107–1116.
Seydoux-Guillaume, A.-M., Bingen, B., Paquette, J.-L., Bosse, V., 2015. Nanoscale evidence for uranium mobility in zircon and the discordance of U–Pb chronometers. Earth Planet. Sci. Lett. 409, 43–48.
Skrzypek, E., Sakata, S., Sorger, D., 2020. Alteration of magmatic monazite in granitoids from the Ryoke belt (SW Japan): processes and consequences. Am. Mineral. 105 (4), 538–554.
Soman, A., Geisler, T., Tomaschek, F., Grange, M., Berndt, J., 2010. Alteration of crystalline zircon solid solutions: a case study on zircon from an alkaline pegmatite from Zomba–Malosa, Malawi. Contrib. Mineral. Petrol. 160 (6), 909–930.
Spier, C.A., Ferreira Filho, C.F., Daczko, N., 2022. Zircon U-pb isotopic and geochemical study of metanorites from the chromite-mineralised Bacuri Mafic-Ultramafic Complex: insights of a Paleoarchean crust in the Amapá Block, Guyana Shield, Brazil. Gondwana Res. 105, 262–289.
Spier, C.A., Ferreira Filho, C.F., Daczko, N., 2022. Zircon U-Pb isotopic and geochemical study of metanorites from the chromite-mineralised Bacuri Mafic-Ultramafic Complex: insights of a Paleoarchean crust in the Amapá Block, Guyana Shield, Brazil. Gondwana Res. 105, 262–289.
Spier, C.A., Daczko, N.R., Zhou, R., 2024. Zircon coupled dissolution-precipitation textures distinguish xenocrystic cargo from rare magmatic zircon in the Paleoarchean Bacuri Mafic-Ultramafic layered Complex, Brazil. Precambrian Res. 404, 107342.
Spruzeniece, L., Piazolo, S., Daczko, N., Kilburn, M., Putnis, A., 2017a. Symplectite formation in the presence of a reactive fluid: insights from hydrothermal experiments. J. Metamorph. Geol. 35 (3), 281–299.
Spruzeniece, L., Piazolo, S., Maynard-Casely, H.E., 2017b. Deformation-resembling microstructure created by fluid-mediated dissolution–precipitation reactions. Nat. Commun. 8 (1), 1–9.
Stuart, C.A., Piazolo, S., Daczko, N.R., 2016. Mass transfer in the lower crust: evidence for incipient melt assisted flow along grain boundaries in the deep arc granulites of F iordland, N ew Z ealand. Geochem. Geophys. Geosyst. 17 (9), 3733–3753.
Timms, N.E., Kinny, P.D., Reddy, S.M., 2006. Enhanced diffusion of uranium and thorium linked to crystal plasticity in zircon. Geochem. Trans. 7 (1), 1–16.
Tomaschek, F., Kennedy, A.K., Villa, I.M., Lagos, M., Ballhaus, C., 2003. Zircons from Syros, Cyclades, Greece—recrystallization and mobilization of zircon during high-pressure metamorphism. J. Petrol. 44 (11), 1977–2002.
Trail, D.S., 1970. Geological Traverses on the Mac. Robertson Land and Kemp Land Coast. Antarctic Division, Department of Supply.
Van Leeuwen, A.T.D.V., Morrissey, L.J., Kelsey, D.E., Raimondo, T., 2019. Recognition of Pan-African-aged metamorphism in the Fisher Terrane, central Prince Charles Mountains, East Antarctica. J. Geol. Soc. Lond. 176 (4), 785–798.

Van Leeuwen, A.T.D.V., Morrissey, L.J., Raimondo, T., Hand, M., 2022. Prolonged high thermal gradient metamorphism in the Curnamona Province, south-central Australia, during the latter stages of Nuna assembly. Precambrian Res. 378, 106775.
Varga, J., Raimondo, T., Daczko, N.R., Adam, J., 2020. Experimental alteration of monazite in granitic melt: variable U–Th–Pb and REE mobility during melt-mediated coupled dissolution-precipitation. Chem. Geol. 544, 119602.
Vermeesch, P., 2018. IsoplotR: a free and open toolbox for geochronology. Geosci. Front. 9 (5), 1479–1493.
Weinberg, R.F., et al., 2020. Decoupled U-Pb date and chemical zonation of monazite in migmatites: the case for disturbance of isotopic systematics by coupled dissolution-reprecipitation. Geochim. Cosmochim. Acta 269, 398–412.
White, R.W., Clarke, G.L., 1993. Timing of Proterozoic deformation and magmatism in a tectonically reworked orogen, Rayner Complex, Colbeck Archipelago, east Antarctica. Precambrian Res. 63 (1–2), 1–26.
Whitney, D.L., Evans, B.W., 2010. Abbreviations for names of rock-forming minerals. Am. Mineral. 95 (1), 185–187.
Young, D.N., Black, L.P., 1991. U-Pb zircon dating of Proterozoic igneous charnockites from the Mawson Coast, East Antarctica. Antarct. Sci. 3 (2), 205–216.
Young, D., Ellis, D., 1991. The intrusive Mawson charnockites: evidence for a compressional plate margin setting of the Proterozoic mobile belt of East. Geol. Evol. Antarct. 1, 25.
Young, D., Zhao, J.-X., Ellis, D., McCulloch, M., 1997. Geochemical and Sr–Nd isotopic mapping of source provinces for the Mawson charnockites, east Antarctica: implications for Proterozoic tectonics and Gondwana reconstruction. Precambrian Res. 86 (1–2), 1–19.
Zhao, Y., Liu, X., Liu, X., Song, B., 2003. Pan-African events in Prydz Bay, east Antarctica, and their implications for east Gondwana tectonics. Geol. Soc. Lond. Spec. Publ. 206 (1), 231–245.